How to Measure the Oxidation State of Multivalent Elements in Minerals, Glasses, and Melts?

Daniel R Neuville, Maria Rita Cicconi, Charles Le Losq

13

How to Measure the Oxidation State of Multivalent Elements in Minerals, Glasses, and Melts?

Daniel R. Neuville[1], Maria Rita Cicconi[1], and Charles Le Losq[1,2]

ABSTRACT

All natural materials and most manufactured technologically relevant materials contain a variable but consequent amount of multivalent elements, like iron. Many physicochemical properties of materials highly depend on the type of multivalent cations they contain, as well as on the concentrations and redox states of those multivalent elements. For instance, color is probably the most visible characteristic, resulting from the presence of multivalent transition elements. Other properties like viscosity and density of liquids are affected by those elements, and, as such, they can be seen as important variables for geologic and industrial phenomena.
The present contribution focuses on providing an overview of the most common techniques currently in use for the investigation of multivalent elements in natural and industrial materials. It covers both destructive and non-destructive methods, as well as element-specific and bulk techniques.

13.1. INTRODUCTION

Nowadays, several techniques are available for material and elemental characterizations, and, sometimes, it is difficult to decide which method is the most appropriate to obtain the often desired and always necessary information. In most cases, the use of various different methods will provide the necessary information required to understand the connections between macro- and micro-scale properties. In this framework, measuring the redox potential and in turn assessing the redox chemical equilibria of multivalent elements is critical for understanding chemical processes. In this short, non-exhaustive chapter, we will present traditional techniques for measuring the redox ratio of an element, such as wet chemistry analyses, electron microprobe, Mössbauer spectroscopy, and optical spectroscopy. We will also present new developments that now allow performing in situ measurements, like X-ray absorption spectroscopy and Raman spectrometry. We will mention the advantages, disadvantages, and the accuracy of each technique, and provide some advices for their use on this basis. For a detailed review of each of the hereabove mentioned techniques, readers are referred to, e.g., Rossman (1988, 2014), Mottana (2004), Wildner et al. (2004), Henderson et al. (2014), Neuville et al. (2014), and de Ligny and Möncke (2019).

13.2. WET-CHEMICAL ANALYSES

Wet-chemical analyses are an old and classic method. Almost all classic chemistry textbooks (e.g., Pascal, 1958; Charlot, 1969) mention different recipes for analyzing chemical composition of, and the average oxidation

[1]*Géomatériaux, CNRS-IPGP, Université de Paris, 1 rue Jussieu 75005 Paris, France*
[2]*Research School of Earth Sciences, Australian National University, Building 142 Acton ACT 2601, Australia*

Magma Redox Geochemistry, Geophysical Monograph 266, First Edition.
Edited by Roberto Moretti and Daniel R. Neuville.

DOI: 10.1002/9781119473206.ch13

state of, multivalent elements in minerals and bulk rock samples. Wet-chemical analyses can be done on liquids or solids (crystal or glass). They are based on the measurement of the concentration of a species in a solution with oxido-reduction properties. The dosing reaction must be:
• quantitative, i.e., the difference of redox potential between the two pairs must be adequate;
• unique, i.e., there should not be other species able to react with the titrant solution or the species formed;
• and fast, to be sure that no other reactions can occur.

At equivalence, the reagents are mixed in stoichiometric proportions, i.e., the number of electrons that can be captured by the oxidant is equal to the number of electrons that may be transferred from the reducer. The detection of equivalence can be achieved in different ways:
• one of the reagents or one of the products is colored (MnO_4^-, I_2…) and the appearance of the color of the product or the disappearance of the color of the reagent indicates equivalence;
• monitoring the evolution of the potential of oxido-reduction couples, the equivalence of which translates into a potential jump;
• using oxido-reduction indicator, which changes color at a defined potential. We can differentiate two sorts of indicators: (i) general redox indicators like substances that change color when they are in the oxidized or reduced forms; (ii) specific indicators that is a new colored chemical species formed as result of the association between the indicator group and the oxidized or reduced species.

In the rest of this section, we will focus on a method, adapted from Wilson (1960), which is fast and easy to perform, and allows analyzing iron in glasses and minerals with a small amount of starting material. It is important that the analysed material is homogeneous, and is not composed of a mixture of glass and crystal or of different minerals, because otherwise the result will be a convolution of the different redox states of the different phases.

This method is composed of two steps. The first step consists in the determination of Fe^{2+}, while the second one consists in measuring the total quantity of iron.

Step 1. Determination of Fe^{2+} (expressed as FeO) by volumetric measurement. It consists in, first, performing a dissolution of the sample in acids, and then measuring the concentration of FeO in the newly formed solution with a titrated solution of $K_2Cr_2O_7$. The recipe is:
• in a platinum crucible, add 0.5 g of crushed glass with 7 ml of sulfuric acid, H_2SO_4, and 3 ml of hydrofluoric acid, HF;
• place the crucible on a Bunsen burner, and maintain boiling for 3 minutes;
• pour the contents of the crucible and the rinsing water into a beaker containing 1 g of boric acid H_3BO_3, 10 ml of sulfuric acid H_2SO_4 diluted to 50 % by volume, and 5 ml of orthophosphoric acid H_3PO_4. Boric acid will neutralize the HF in the solution, while sulfuric acid makes our solution more acidic. Phosphoric acid will form a complex with iron;
• add a few drops of colored indicator. In the present recipe we use diphenylamine barium sulfonate. The solution is then dosed by gradually adding a titrated solution of dichromate potassium $K_2Cr_2O_7$ and identifying the shift of the color of the solution to purple (provided by the indicator).

The ferrous iron content present in the solution is deduced from the volume, V, of $K_2Cr_2O_7$ required to obtain the purple color shift and the mass, m, of dissolved glass:

$$\%FeO = 100*2V/m*M_{FeO}/M_{Fe} \qquad (13.1)$$

where M_{FeO} and M_{Fe} are the molar mass of FeO and Fe. This gives the final equation:

$$\%FeO = 257.3*V/m. \qquad (13.2)$$

Step 2. Determination of total iron (expressed as Fe_2O_3) by volumetric measurement. This step consists in the reduction and the determination of all the iron in the sample using a titrated solution of $K_2Cr_2O_7$. The recipe is:
• in a platinum crucible, mix 1 g of sample, 40 ml of HF, and 5 ml of H_2SO_4;
• heat the solution on a Bunsen burner until total evaporation;
• add 2 g of boric acid H_3BO_3 and 5 ml of H_2SO_4 to the residues;
• heat the solution again for about 30 minutes;
• pour the contents of the crucible and the rinsing water into a beaker. Keep the solution
• boiling until it clears up;
• reduce the volume of solution to 500 ml with distilled water. Take 50 ml of solution (~ 0.1 g of sample) and pour into a beaker;
• to these 50 ml, add 5 ml of sulfuric acid, 2 or 3 drops of arsenio-tungstate, $(AsO_4\ (WO_3H_3)_9)_2$, a few drops of $TiCl_3$ until the solution's color shifts to blue;
• pour potassium dichromate until the color fades, which corresponds to complete oxidization of $TiCl_3$;
• add 5 ml of acid phosphoric, H_3PO_4, and a few drops of barium diphenylamine sulfonate, $C_{24}H_{20}BaN_2O_6S_2$;
• this solution is dosed with potassium dichromate, $K_2Cr_2O_7$.

The total iron content present is deduced from the volume V of potassium dichromate necessary to observe the color shift, and from the mass m of initial glass/mineral via the equation:

$$Fe_{tot} = 20V/m*M_{Fe2O3}/2M_{Fe}, \qquad (13.3)$$

where M_{Fe2O3} and M_{Fe} are the molar mass of Fe_2O_3 and Fe, respectively. This yields the final equation:

$$Fe_{tot} = 2859.3 * V/m. \quad (13.4)$$

Thus, knowing the total iron content (expressed as Fe_2O_3), the actual Fe_2O_3 content of the sample can be calculated as:

$$\%Fe_2O_3 = Fe_{tot} - \%FeO * M_{Fe2O3}/2M_{FeO}, \quad (13.5)$$

which corresponds to:

$$\%Fe_2O_3 = Fe_{tot} - 1.1113 * \%FeO. \quad (13.6)$$

Advantages, drawbacks, accuracy

Wet chemistry is an old technique with the following advantages:

- *it is an absolute method;*
- *it is very accurate technique, generally more than ±0.05, and in the case of iron redox ± 0.02 on the Fe^{3+}/Fe^{2+};*
- *it can be used to analyze the concentration and oxidation state of a wide variety of chemical elements.*

However, it presents some major drawbacks, preventing its widespread adoption:

- *it requires handling potentially dangerous and/or toxic reagents or acids;*
- *it usually requires a large amount of sample (more than 1 gram);*
- *it is destructive;*
- *of course, it is not possible to map the redox ratio of an element in a sample.*

13.3. ELECTRONIC MICROPROBE

Electron microprobe, like wet chemistry, allows analyzing a sample chemical composition, with the exception of light elements. In addition to major element composition, several studies also focused on developing this method for the analysis of the oxidation state of iron in minerals and glasses.

The first tests to determine the iron redox ratio with electron microprobe date back to the 1960s. In particular, the works of Fisher (1965) and Albee and Chodos (1970) can be mentioned. Iron has unfilled 3d states ($3d^5$ for Fe^{3+} and $3d^6$ for Fe^{2+} unlike $3d^{10}$ for the filled level). The peaks of the L series emitted from the metals of first order transition are the result of electronic transitions between the 3d orbitals partially filled and the 2p core levels ($L_{2,3}$). Different methods are based on the analysis of the Fe $L_{\alpha,\beta}$ emission spectra of minerals and glasses to measure their Fe^{3+}/Fe^{TOT} (Höfer et al., 1994, Fialin et al., 2001, 2004, Zhang, Almeev, et al., 2018; Hughes et al., 2018, 2020).

One method for determining Fe^{3+}/Fe^{TOT} is based on the difference in the self-absorption effects on both Fe^{2+} and Fe^{3+} L_α peak positions (Höfer et al., 1994). Self-absorption is the absorption by a chemical species of its own X emissions characteristics. The position, shape, and intensity of the Fe L_α peak all depend strongly on whether Fe in the sample is predominantly Fe^{3+} (low self-absorption) or Fe^{2+} (strong self-absorption). From this point, three approaches allow estimation of the iron redox ratio from the Fe $L_{\alpha,\beta}$ spectra:

- measurement of the energy displacement of the L_α peak (Fialin et al., 2001, 2004);
- measurement of the L_β/L_α intensity ratio (Albee and Chodos, 1970);
- a mixed method developed by Höfer et al. (1994).

Advantages, drawbacks, accuracy

The electron microprobe can be a good tool to measure the Fe redox ratio in glasses because:

- *it also allows, in parallel, to perform a full chemical analysis of the material;*
- *local analysis and mapping are possible;*
- *it is fast and easy to perform, as in most cases samples will eventually be mounted in epoxy and analyzed by electron microprobe (but this can also be a drawback in some cases, listed here).*

However, this method presents various drawbacks:

- *accuracy on the Fe^{3+}/Fe^{TOT} redox ratio is of around ± 10 %;*
- *it requires some sample preparation, including polishing and metallization of epoxy sample mounts;*
- *samples should contain a maximum of 15 wt% of light elements that tend to migrate under the beam, like sodium or boron;*
- *good measurements require high iron content, ~3–4 wt% of total iron minimum;*
- *chemical and redox analyzes of glasses with volatile elements are problematic.*

13.4. MÖSSBAUER SPECTROSCOPY

Mössbauer spectroscopy is one of the common tools for determining the redox ratio and the coordination of iron in silicate glasses (Mysen et al., 1980, 1985; Mysen, 1985; Jayasuriya et al., 2004; Zhang, Cottrell, et al., 2018; Cottrell et al., 2018; Gaborieau et al., 2020). Mössbauer spectroscopy made recently some very important progress through new notable developments on synchrotron light source. Such developments allow measuring the oxidation state of an element *in situ* in a diamond anvil-cell, for example. This can provide very important direct knowledge regarding the iron redox ratio and environment at

conditions pertinent for the Earth interior (Potapkin et al., 2012; Cerantola et al., 2017; Maeda et al., 2017; Wei et al. 2017; Cottrell et al., 2018).

Mössbauer spectroscopy is an element-specific technique. It is based on the Mössbauer effect, named after R. L. Mössbauer who received the Nobel prize in 1961 for his discovery. The Mössbauer effect is a phenomenon of nuclear resonance that affects specific isotopes (^{57}Fe, ^{119}Sn, ^{121}Sb, ^{125}Eu). It is apparent in the gamma ray region of the electromagnetic spectrum. A radioactive source emits γ radiation following de-excitation mechanisms of the nucleus between its excited state and its ground state. The gamma radiation emitted is then absorbed by the sample. It probes tiny changes in the energy levels of an atomic nucleus in response to its environment (electric, magnetic, chemical, redox, ligand, etc.). Typically, three types of nuclear interactions may be observed: (i) isomer shift, also called chemical shift in the older literature; (ii) quadrupole splitting; and (iii) magnetic hyperfine splitting. Observation of those phenomena provides information on the charge, spin, and local symmetry of the probed atom, as well as on its internal electric and magnetic fields.

The sample emits a modulated signal, which represents itself as a displacement in energy of the absorption band of the spectrum with respect to the emission energy. The energy displacement of the absorption line with respect to the emission line is named isomer displacement (δ or IS). As it is related to the electronic density of the nucleus, δ is an indicator of its valence. On the other hand, the interaction of the quadrupole moment of the atomic nucleus with the aspherical distribution of electronic charges is presented by a doublet and called quadrupole interaction (Δ or QS). The separation between the two peaks of the doublet is a measure of this interaction. In the case of iron, it is associated with the asymmetry of the environment of the nucleus of iron, and, therefore, informs about the coordination of iron.

An example of a Mössbauer spectrum of iron in a diopside glass with 10 % Fe_2O_3, prepared in slightly reducing conditions at high temperature, is shown in Fig. 13.1. After decomposition of the observed peaks into different components (Lorentzian functions), the relative areas of signals assigned to ferric and ferrous iron are calculated. The redox ratio can be estimated from the ratio of those areas. Spectra of reduced and oxidized samples have an asymmetrical and a symmetrical doublet, respectively. Charts linking isomer displacement and interaction quadrupole provide the coordination of iron.

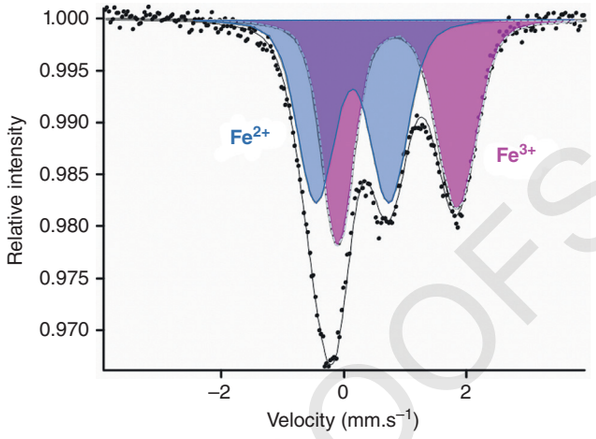

Figure 13.1 Mössbauer spectra of an Fe-bearing diopside glass prepared at 1500 °C, under slightly reducing conditions (log fO_2 = –2.65). Round dots are the experimental measured signal, fitted by the mathematical functions with blue and pink colors, which represent, respectively, the Fe^{2+} and the Fe^{3+} contributions (redraft from Roskosz et al., 2008).

Advantages, drawbacks, accuracy

Mössbauer spectroscopy has the following advantages:

- *it is very accurate, precision is +/– 0.02 Fe^{3+}/Fe^{TOT}*
- *it is an absolute method;*
- *it does not involve extensive chemical manipulations of the samples;*
- *thanks to the advances in synchrotron radiation (Potapkin et al. 2012), microbeam are now available and allow in-situ, non-destructive spatially resolved measurements.*

However, it also has several drawbacks:

- *only a few elements are accessible for redox measurements;*
- *a large number of samples are needed (excluding synchrotron developments);*
- *it is a destructive method (excluding synchrotron developments);*
- *it involves low temperature measurements (excluding synchrotron developments);*
- *it requires an expensive and time-perishable radioactive source;*
- *signal decomposition and interpretation may be challenging.*

13.5. OPTICAL ABSORPTION SPECTROSCOPY

Optical absorption (OA) techniques allow the identification of electronic transitions in the frequency range 50000 cm^{-1}–2000 cm^{-1}, thus covering the spectral range from ultraviolet (UV) to near-infrared (NIR). It includes the small region that human eyes are able to detect (Visible, VIS) from ~26000 cm^{-1} to ~12800 cm^{-1} (see Fig. 13.2). Specific reviews that describe the basic concepts, the use of this technique in geosciences, or the nature of color in

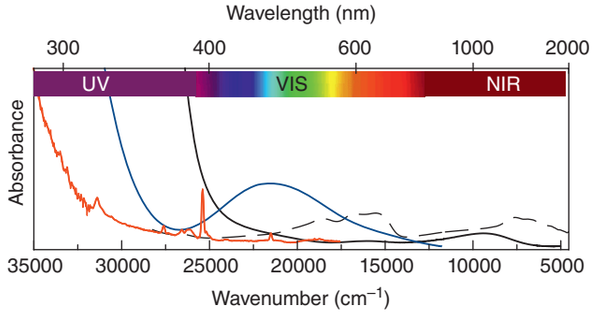

Figure 13.2 Example of Optical Absorption spectra of glasses containing different transition elements: Mn^{3+} doped aluminosilicate glass (blue line); V doped sodium silicate glass (black line); and an archaeological glass containing different multivalent elements (dashed black line). In red, the spectrum of a Eu^{3+}-rich metaphosphate glass (data from Cicconi et al., 2017a). Depending on the absorber(s), bands can be broad or narrow, and occur at different frequencies. On top, the UV–VIS–NIR frequency ranges are reported for reference.

crystalline and amorphous materials are e.g., Wildner et al. (2004), Rossman (2014), and de Ligny and Möncke (2019).

When a radiation interacts with a material, the light can be reflected, scattered, or absorbed. If the outgoing light (with intensity I) has a lower intensity with respect to the incoming beam (with intensity I_0), then the sample has absorbed some of the light. The portion of absorbed light will depend on the thickness of the sample, and on the amount (concentration) of absorbent species. The attenuation of the incident beam intensity I_0, when passing through a sample, is described by the Lambert-Beer equation:

$$I = I_0 \exp(-\mu x), \tag{13.7}$$

with x the thickness of the sample, and μ the linear absorption coefficient that actually depends on the incident wavelength λ. The latter point actually implies that λ intervenes in the Lambert-Beer law described by Equation 13.7 (Wildner et al., 2004).

Using this principle, an UV/VIS or UV/VIS/NIR spectrophotometer measures the intensity I of absorbed or transmitted light as a function of I_0 at each given λ. The ratio $I(\lambda) / I_0(\lambda)$ can be referred to as the transmittance T. In an optically transparent material, $I(\lambda) \sim I_0(\lambda)$ (ignoring reflections), hence the percent transmittance %T will be ~100. On the contrary, a non-transparent material (opaque) will have a %T = 0. The absorbance A is instead defined as:

$$A = \log(I_0(\lambda)/I(\lambda)) = \epsilon C\, x, \tag{13.8}$$

with C the absorber concentration, x the sample thickness, and ϵ the extinction coefficient. Thus, the amount of light absorbed by a material is directly proportional to the concentration of the absorber, and to the length of the light path (Wildner et al., 2004). We can note that when a photon is absorbed by an atom or molecule it passes from the normally occupied lower energy state, often called the ground state, to an upper or excited state. These transitions are, for example, responsible for colors in minerals and glasses. However, it is important to remark that these electronic transitions are much weaker than charge transfer transitions. For instance, one of the most famous examples is the charge transfer occurring in sapphire, where Ti^{4+} and Fe^{2+} can provide the typical blue color, even if present at ppm levels (Dyar et al., 2008).

An example of optical absorption spectrum, in the range 4000–28500 cm^{-1}, of a blue colored archaeological glass is reported in Fig. 13.3. This glass has many chromophore elements, and the strongest electronic transitions can all be seen in the spectrum, with Co, Mn, Cu, and Fe providing clear absorption bands. Other transitions may be too weak to be visible, such as those associated with 6-fold coordinated Mn^{2+} ions. Indeed, the pinkish/reddish color deriving from $^{[6]}Mn^{2+}$ transitions can be really detected only in the mineral rhodochrosite because of its high Mn^{2+} concentration (Rossman, 1988, 2014). Nevertheless, by combining other optical techniques, i.e., photoluminescence spectroscopy, it could be possible to observe both absorption and emission of Mn^{2+} ions, without interference from the oxidized Mn^{3+} species. Another useful technique that could be associated with the optical ones is [KT]EPR spectroscopy (Electron Paramagnetic Resonance) [\KT]. EPR reveals the signal only of species having unpaired electrons (e.g., V^{4+}, Mn^{2+}, Fe^{3+}, Cu^{2+}), thus it allows discriminating many different transition elements (Möncke et al. 2014).

Despite all chromophore elements present in this example, the resulting glass has the typical deep blue color of

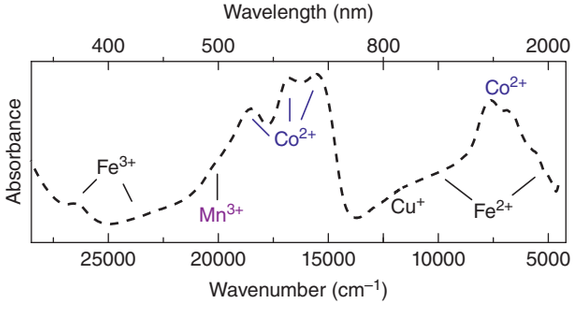

Figure 13.3 Optical absorption spectrum, in the range 4000–28500 cm^{-1}, of a deep blue colored glass. The color is mainly provided by $^{[4]}Co^{2+}$ ions, but several other broad bands are visible as evidence of the presence of other transition elements.

Co^{2+} 4-fold coordinated. All *d–d* transitions are Laporte-or parity-forbidden (Laporte parity selection rule), which reduces the transition probabilities and, in turn, the absorption intensity (intensity of the transitions). However, the Laporte rule can be relaxed (weakened) for non-centrosymmetric geometries, and as a result, high-absorption intensities are associated with the absorption bands of $^{[4]}Co^{2+}$ ions (Möncke et al. 2014; Moncke 2018).

As observed in the previous examples, optical absorption techniques are very sensitive and allow to detect the presence of many elements, even at very dilute levels. However, the quantification of the average oxidation state is very challenging for most of the chemical elements. For example, in the archaeological glass reported in Fig. 13.3, the presence of various broad transitions associated with the different elements introduced in the glass hampers any significative quantification of the redox state (Cicconi et al., 2020). Ergo, often many other techniques are coupled to optical absorption measurements, in order to obtain complementary information (XAS, photoluminescence, XPS, voltammetry, and titration are some examples) (e.g., Leister et al., 1999: Bingham et al., 2002; Möncke et al., 2014; Hunault et al., 2016). Furthermore, even in the case of a simplified bulk composition having a single transition element, the extraction of useful information is not always straightforward, since the appropriate extinction coefficients must be available.

An example of this complexity is reported in Fig. 13.4, where the absorption spectrum of an aluminosilicate glass doped with vanadium is reported. Vanadium in glasses can be stable with three possible valences, V^{5+}, V^{4+}, and V^{3+}, that provide a variety of responses in terms of optical properties (electronic configuration varies from $3d^0$ to $3d^2$) and several bands in the UV-VIS-NIR region. Moreover, V^{5+} species do not provide electronic transitions because of the $3d^0$ electronic configuration. Thus, only charge transfer bands occur that overlap the UV-edge. In order to evaluate the distinct extinction coefficients that are needed to quantify the proportions of the different V species from the absorption spectra, Leister et al. (1999) performed the signal deconvolution of several glasses (an example of signal deconvolution is reported in Fig. 13.4) but also required other techniques. For example, the extinction coefficients of reduced V^{3+} can be obtained from the deconvoluted optical absorption spectra of glasses synthesized at very reducing conditions, where V^{3+} are the only (or predominant) ions present. However, in order to determine the concentration of V^{4+} species and, in turn, to calculate the extinction coefficients for V^{4+}, the authors used other techniques, such as Square-wave voltammetry and Electron Spin Resonance (Leister et al. 1999).

Thus, by using optical absorption, it is possible to quantitatively obtain information on an element oxidation state, along with information on coordination, bonding character and site geometry. Moreover, the high sensitivity of this technique allows detecting species at very low concentrations. Despite that, the use of other spectroscopic or voltammetry techniques is often required for an accurate determination of the proportions of the different redox species.

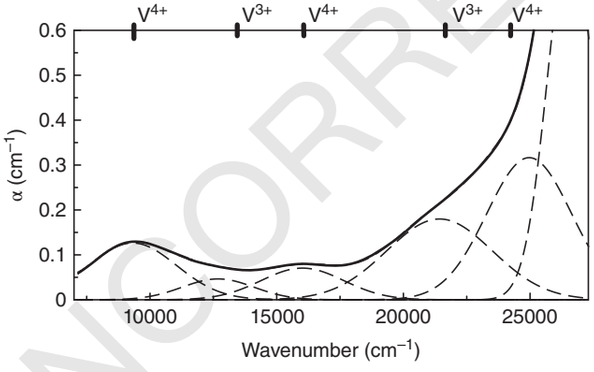

Figure 13.4 Optical Absorption spectrum of a V-doped sodium aluminosilicate glass melted at 1400 °C, in air (1.8 mol% V_2O_5) in the frequency range 7000–27300 cm^{-1}. Several broad bands associated with electronic transitions of V^{4+} and V^{3+} species are visible. V^{5+} charge transfer band(s) are not discernible from the UV-edge. Dashed lines represent the mathematical functions used for signal deconvolution. The proportions of the different redox species can be calculated by using the appropriate extinction coefficient and the area of the deconvoluted bands. Modified after Cicconi et al. (2020).

Advantages, drawbacks, accuracy

Optical Absorption spectroscopy is regularly used in, e.g., analytical chemistry for a qualitative and quantitative determination of different analytes, either in liquid, solid or gas form. In Geosciences, it is widely used to study crystalline and amorphous solids containing transition elements and lanthanides. This technique has several advantages:

- *OA has high accuracy and it is a cost-effective method;*
- *it can provide information not only on the type of species, but also on their local environment (oxidation state, bonding character, coordination);*
- *OA can be also a quantitative technique, and, in simplified systems, absorber concentration can be derived from the Lambert-Beer's equation;*
- *it has high sensitivity.*

On the other hand, it is important to point out that the measured signals can be very weak, and the signal/noise ratio of the collected signals may be very low. Thus, a good calibration of the instrument is required in order to remove the noise characteristic of the source, and the electronic noise from the detector. Furthermore, for classical transmission measurements, the sample preparation can be time

consuming (e.g., optical-grade quality double-sided polishing), and opaque samples must be measured in reflectance mode. Finally, the analysis of natural samples can sometimes be very tricky because of the overlap of many different electronic and charge transfer transitions that may occur in a single sample.

13.6. X-RAY ABSORPTION SPECTROSCOPY

[KT] X-ray Absorption Spectroscopy (XAS) [\KT] is an element-specific spectroscopic technique that allows studying many elements of the periodic table, in many types of phases (crystalline, amorphous, liquids, gases). It provides information on the electronic, structural, and magnetic properties of the sample. Detailed information about the theory as well as data acquisition and reduction protocols for materials can be found in these contributions: Brown et al. (1988), Mottana (2004), Henderson et al. (2014), and Willmott (2011). Moreover, the readers are encouraged to read the recent paper by Abe et al. (2018) to have an overview of the different XAS-based techniques, applications (catalysis, high-pressure), and sources of errors.

XAS is a measurement of the variation of the linear X-ray absorption coefficient $\mu(x)$ as a function of the X-ray energy E. The incident x-ray beam has an energy $E = h\nu$, (E in keV, h is Planck's constant, ν is the frequency) and an intensity I_0. A typical detection mode of the XAS signal is based on transmission measurements, hence on the attenuation of the incident beam intensity when passing through a sample. It follows the Lambert-Beer's law (see Section 13.5, Equation 13.7). However, depending on the X-ray energy range selected, on the element investigated (photoabsorber), on the concentration of the photoabsorber, and on the matrix, there are other detection methods that can be used, i.e., fluorescence and [KT] total-electron-yield (TEY) [\KT]. For instance, thin concentrated samples should be collected in transmission mode, whereas dilute, low-energy edges are better detected with fluorescence measurements. Details on the instrumentations, and on the different acquisition modes, are provided in Van Bokhoven and Lamberti (2016).

The X-Ray absorption spectrum of an element, usually displayed as a function of X-rays energy, can be divided into three regions with increasing energy, as shown in Fig. 13.5 (e.g., Natoli and Benfatto, 1986; Mottana, 2004; Bunker, 2010; Willmott, 2011):

1. a pre-edge region occurring at energies lower than the absorption peak (2–20 eV before the absorption edge), i.e., where the incident X-ray energy E is lower than the binding energy E_b, of an electron in the orbital, $E < E_b$,

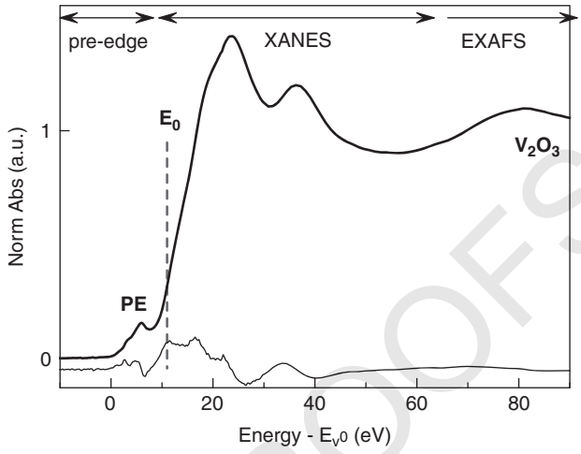

Figure 13.5 Energy scaled K-edge XAS spectrum of vanadium in divanadium trioxide (V_2O_3). The main sub-regions are reported: the pre-edge region before the absorption edge (E_0) that contains the small feature PE (pre-edge peak); the multiple scattering region (XANES) that extends from several eV above the pre-edge up to ca. 50 to 70 eV above the edge; and the single scattering region or extended region (EXAFS). On the bottom, the first derivative of the spectrum is reported. E_0 identifies the edge position, and is defined as the first maximum of the first derivative function. E_{V0} = metallic V K-edge = 5465 eV.

and electronic transitions have low probabilities (Geiger, 2004; Van Bokhoven and Lamberti, 2016). A feature (pre-edge peak, PE) may be present. It is linked to the crystal field transition, and, in the case of K-edge transitions of *3d* transition elements, it derives from the *1s* to the empty *3d* levels more or less *4p* hybridized by the ligands (*1s* ➔ *3d*-like levels transition);

2. when the X-ray incoming energy approaches the binding energy ($h\nu \sim E_b$) there is a higher probability for an electronic transition to occur, resulting in an absorption edge. This region is called the [KT] X-ray Absorption Near Edge Structure or XANES [\KT] region and is characterized by sharp absorption structures arising from strong multiple scattering of photoelectrons by atoms surrounding the absorber. This scattering process involves multiple scattering centers that often extend beyond the first nearest-neighbor shell of ligands (Geiger, 2004; Bunker, 2010; Willmott, 2011; Van Bokhoven and Lamberti, 2016);

3. The third region of the spectra, extending from about 50 to 1000 eV above the edge, is called the [KT] Extended X-ray Absorption Fine Structure, namely EXAFS [\KT] region and it is characterized by weak oscillations of the spectrum due to backscattering of the photoelectrons (Geiger, 2004).

Since each region is characterized by distinct phenomena, particular care must be taken when using acronyms.

Indeed, many authors misuse the terms XAS, XANES, and EXAFS, and sometimes they are erroneously considered synonymous. From a redox point of view, the first two regions are the ones providing key information regarding an element oxidation state.

XANES covers the range between the threshold (E_0) and the point at which the EXAFS region begins. Because of its origin, XANES is particularly sensitive to the geometrical arrangement of the first neighbors around the central absorber. As a consequence, it provides information on site geometry, symmetry, and bond angles, as well as knowledge about the oxidation state of the absorber. Beyond the absorption edge, the EXAFS region is used to ascertain geometrical parameters such as the interatomic distances between the investigated absorbing atoms and the neighbors in its immediate surrounding, the coordination number with the nearest and next-nearest neighbors and their nature (Galoisy, 2004, and references therein; Henderson et al. 2014).

13.6.1. K-edge XANES Spectra of *3d* Transition Elements

The analysis of the XANES region is widely used in many scientific fields. It provides information about the average valence and coordination number of an elements, as well as the type of ligands and site symmetry. Since the 1980s, many mineralogical, geochemical, and environmental studies are based on XANES spectra at the K-edge (*1s*). These early studies favored the first-raw transition elements since it was possible to obtain spectra with good signal/noise ratio and high energy resolution in air, despite moderately powerful second-generation synchrotron radiation (Mottana, 2004). In particular, K-edge XANES spectra of *3d* transition elements present spectral features and energy shifts that can provide excellent structural information on the photoabsorber in glasses and minerals. Indeed, the pre-edge peak and the edge structures can be used to derive information on the photoabsorber speciation without an exhaustive theoretical work. Information can be extracted using empirical correlations, built from the study of XANES spectra acquired on reference materials with well-known local structure (see Section 13.6.2).

To briefly illustrate the variations occurring in the XANES region depending on element valence and ligand geometry, spectra for some of the first-row transition metal oxides are reported in Fig. 13.6, in the energy range covering the pre-edge peak region up to ca. 50 eV above the absorption edge (E_0). The spectra show many variations depending on the element speciation. For example, the vanadium oxides XANES spectra reported in Fig. 13.5 present a wide range of oxidation state (0 to +5); these yields absorption edge shifts to higher energy with increasing oxidation state, from ~5465 eV for V^0 to ~5480 eV for V^{5+}. Besides oxidation state information, V coordination geometries can be deduced as well from the spectra and Wong et al. (1984) reported a very detailed study of Vanadium oxides. For instance, the V site shows regular octahedral symmetry Oh in VO, but distortion increases from C3 in V_2O_3 to C_s in V_2O_5 (Wong et al. 1984); such changes go along with the pre-edge peak rising in intensity following the loss of symmetry. In detail, VO has a NaCl cubic face-centered structure with regular octahedral VO_6 units. In this structure, the electronic transition $1s \rightarrow 3d$ is dipole-forbidden, resulting in a weak (or virtually zero) pre-edge peak. On the contrary, when the inversion center is broken, due to the loss of symmetry, as in the case of the distorted 6-fold coordinated VO_6 units in V_2O_3, the pre-edge peak increases its intensity. V_2O_5 displays V in 5-fold coordination in highly distorted tetragonal pyramids, and presents a very strong pre-edge peak (Wong et al. 1984). Thus, the crystal field theory could be used to provide an interpretation of the pre-edge peak characteristics (de

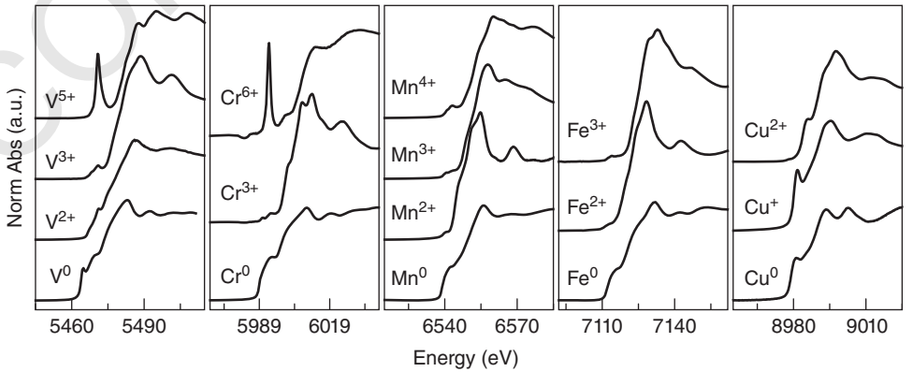

Figure 13.6 XANES spectra of first- row multivalent transition metal oxides (except Cr^{6+} compound: $CaCrO_4$). The spectra follow similar trend with the shift of the absorption edge to higher energies at increased average oxidation state.

Groot et al. 2009) and, in theory, the highest pre-edge peak intensity is reached in case of tetrahedral coordination (T_d).

The other transition element oxides shown in Fig. 13.6 follow similar trends, showing a shift of E_0 to higher energy at increased oxidation state, and a correlation between pre-edge peak intensity and local site symmetry. Cr K-edge XANES spectra are discussed in detail in Bell et al. (2020, this volume).

13.6.2. Extracting Information from XANES Spectra

In order to extract information on elements average oxidation state and local environment from the XANES region, several approaches can be adopted depending on the element studied as well as on the electronic transition considered (e.g., K- or L-edge). Here we will report a few examples on: (i) absorption edge position; (ii) absorption edge and pre-edge peak; (iii) signal deconvolution; and (iv) linear combination. The first two methods are mainly based on the empirical approaches, and thus, based on the study of reference materials with well-known structure.

A basic procedure to determine the average oxidation state of a multivalent element in materials is to calculate the absorption edge position (hereby referred as the inflection point, E_0) of several well-characterized reference materials. Since there is a shift of E_0 to higher values with increasing the oxidation state (Fig. 13.6), a calibration might be established, and then used to estimate the average valence of unknown samples. This method has often shown to be extremely reliable, as in the case of V oxides (Wong et al., 1984) or Mn oxides (Fig. 13.6; Belli et al., 1980). However, in other cases, the correlation between the formal oxidation state and the absorption edge position is not accurate enough (e.g., Farges, 2005). This is especially the case when the element in the investigated material is present with different coordination geometries and site occupancies. Manganese compounds represent a good example to visualize such complexities. Mn has valences ranging from 0 to +7. The Mn K-edge spectra of the crystalline compounds shown in Fig. 13.7a are representative of the most stable oxidation states in geological systems (2+, 3+, and 4+), and of the different Mn coordination geometries (see Table 13.1). Mn K-edge absorption edge shifts to higher energies upon increasing Mn oxidation state. However, an energy shift can be observed as well when changing the local symmetry around Mn, even at constant oxidation state (e.g., Rodocrosite and MnO). Consequently, in this specific case the simple observation of the edge position is not enough to precisely characterize the samples and supplementary analysis are necessary, such as the detailed study of the pre-edge peaks, or the use of a complementary technique.

XANES spectra of some Fe minerals (Table 13.1) and Fe-bearing silicate glasses are shown in Figs. 13.7b and c (experimental details provided in Giuli et al. 2011, 2012a, b; Cicconi et al. 2015a). The spectra of the Fe crystalline compounds reported here represents the most common stable oxidation states (2+ and 3+) and coordination geometries of Fe in geologic materials. In the case of iron, qualitative and quantitative information on *1s → 3d/4p*

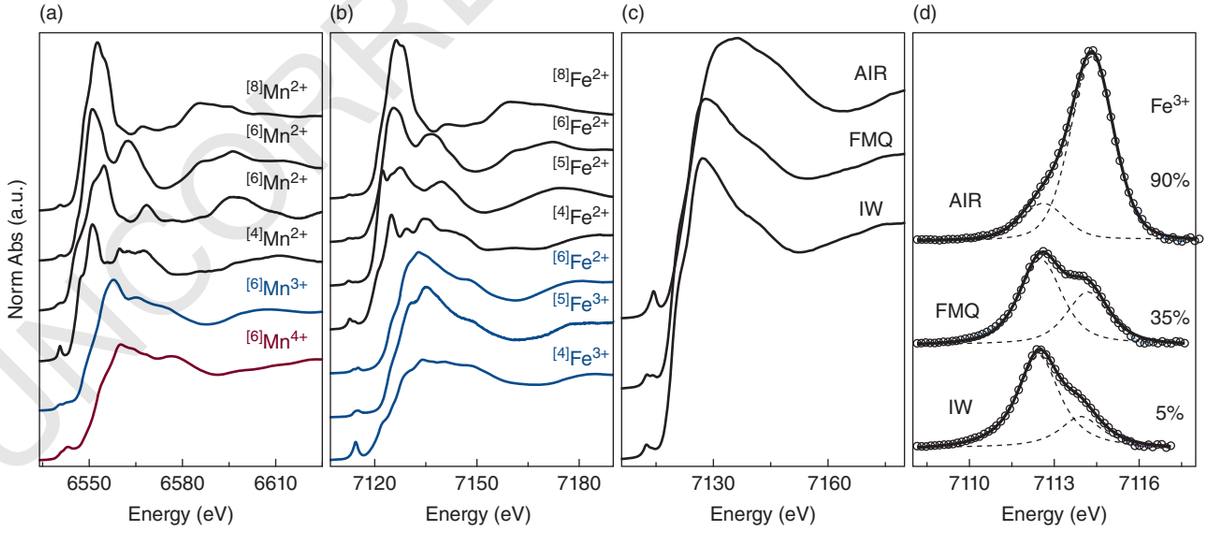

Figure 13.7 K-edge XANES spectra of Mn (a) and Fe (b) crystalline compounds (names listed in Table 13.1). (c) Fe K-edge XANES spectra of silicate glasses equilibrated under different fO_2 conditions. (d) background subtracted pre-edge peaks, and their deconvolution; estimated $\%Fe^{3+}$ are reported (±5 %).

Table 13.1 Fe and Mn crystalline compounds reported in Fig. 13.6. Experimental details for Fe and Mn minerals are reported in Giuli et al. (2011, 2012a, b), and Cicconi et al. (submitted), respectively.

Crystalline compound	Valence	Coordination
Almandine	Fe^{2+}	[6]
Siderite	Fe^{2+}	[6]
Ericaite	Fe^{2+}	[5]
Akermanite	Fe^{2+}	[4]
Aegirine	Fe^{3+}	[6]
Yoderite	Fe^{3+}	[5]
Kimzeyite	Fe^{3+}	[4]
Spessartine	Mn^{2+}	[8]
Rodocrosite	Mn^{2+}	[6]
MnO	Mn^{2+}	[6]
Helvite	Mn^{2+}	[4]
Mn_2O_3	Mn^{3+}	[6]
MnO_2	Mn^{4+}	[6]

transitions were obtained for Fe-bearing crystalline and amorphous materials by e.g., Waychunas et al. (1983), Calas and Petiau (1983), Petit et al., (2001), Berry et al., (2003, 2010), Bajt et al. (1994), Galoisy et al. (2001), and Wilke et al. (2001). Since these studies, several others have shown that it is possible to correlate Fe pre-edge peak features (i.e., intensity and barycenter) with both the average site geometry (and symmetry) and iron average valence state.

In-depth pre-edge analysis requires several steps. After the first step that consists of background subtraction, the pre-edge peak can be decomposed in different peaks with given mathematical functions (e.g., pseudo-Voigt). This allows one to estimate, for example, the PE weighted energy position (a.k.a. centroid or barycenter) and the PE total integrated area (Fig. 13.6d; see Wilke et al., 2001, 2004). For Fe, in known crystalline reference materials, with Fe present with a single valence and in a single crystallographic site, the PE analysis has shown that the centroid position of Fe^{3+} compounds is ~2.4 eV above the edge of metallic Fe (7112 eV), whereas the centroid of Fe^{2+} is at ~0.9 eV above the metallic Fe one. For more complex Fe site geometry, or for mixed valences, there is a nonlinear response between pre-edge peak centroid and integrated intensity (see variogram in e.g., Wilke et al., 2001; Giuli et al. 2012a; Henderson et al., 2014). Fortunately, it is possible to estimate both Fe average oxidation state and coordination number with a good accuracy, by using mixing lines between the end-members (e.g., Wilke et al., 2004). As a result, the determination of the average Fe redox ratio and coordination via the study of the Fe pre-edge peak is very common nowadays.

XAS spectra of glasses present less structures and broader features compared to crystalline materials because of the lack of periodicity in amorphous materials (Fig. 13.7c). Nevertheless, the considerations done for the crystalline compounds are still valid for glasses or liquids. Figs. 13.7c and 13.7d show the Fe K-edge spectra of phonolitic glasses, equilibrated over a range of oxygen fugacity (fO_2) conditions [$\log_{10}(fO_2)$ from –0.68 to –11; from air to FMQ, to IW[1]] (Cicconi et al., 2015a). The absorption edge shifts from 7123.5 eV to 7119 eV with decreasing fO_2 conditions, indicating higher amount of reduced Fe species. In addition, the pre-edge peaks strongly change depending on the fO_2 conditions. The PE peak can be fitted with two pseudo-Voigt functions, whose energies at ~7112.65 and ~7114.4 eV are consistent with those of Fe^{3+} reference materials. For samples prepared in air, the dominant peak at higher energies, is that assigned to Fe^{3+}, while for samples equilibrated under reducing conditions (close to the IW buffer) the dominant one is the peak at lower energies, assigned to Fe^{2+}. The estimated centroids, from air to IW, were: 2.34 eV and 1.04 eV (above the Fe metallic energy), respectively providing estimated Fe^{3+} content of ~90 % and 5 % (±5 %), in agreement with the values quantified via wet-chemistry (Cicconi et al., 2015a). Hence, the deconvolution of the pre-edge peak is a very accurate way to quantify the Fe redox ratio in many materials and in some cases, it has reached an extremely high accuracy (Berry et al., 2018; Zhang, Cottrell, et al., 2018). The same approach can be used for signal collected *in-situ* at high temperatures, and/or under different imposed fO_2 conditions (Magnien et al., 2004, 2008; Cochain et al., 2012; Cicconi et al., 2015b).

We have shown that both the absorption edge position and the analysis of the pre-edge peak may provide a satisfactory assessment of an element valence and local environment. However, natural materials, either crystalline or amorphous, usually present a higher complexity in the transition element local environment, making the interpretation of the different XANES spectral features difficult. Furthermore, for many multivalent elements, it is not always possible to perform studies based on crystalline reference materials, simply because they may not be available (e.g., no natural Ti^{3+} or Eu minerals are available). Moreover, the detailed study of edge and pre-edge features require the use of a monochromator that provides high energy resolution. This induces some drawbacks in term of acquisition setup for the acquisition of very good spectra in the extended region.

Other ways to gather information from the XAS data imply peak fitting of the spectral features, and/or the linear combination of two end-members. Spectral peak fitting is a time-consuming procedure, which involves the knowledge of the electronic transitions responsible for the XANES

[1] Respectively, fayalite-magnetite-quartz, and iron-wüstite buffers

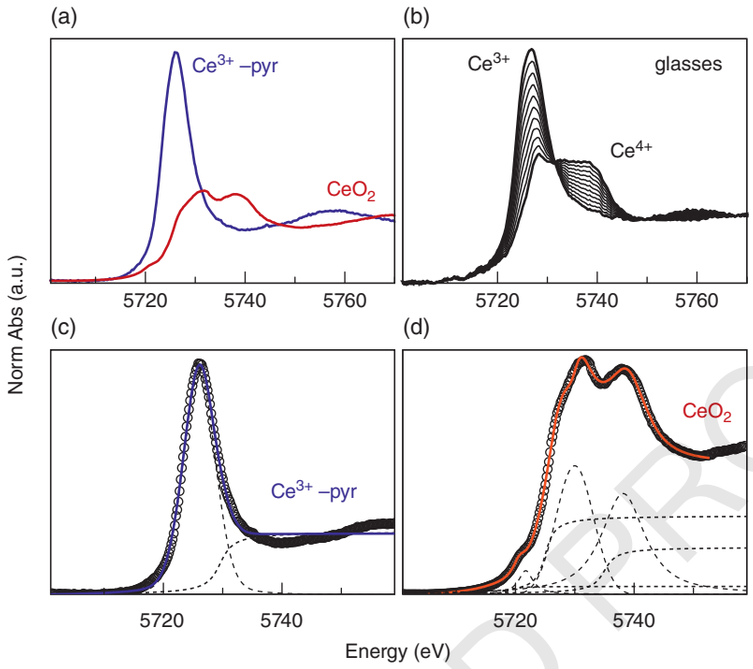

Figure 13.8 Cerium L_{III}-edge XANES spectra for two Ce crystalline materials (a), and examples of linear combination (b) and deconvolution of the spectral features (c and d). See text for details.

features. However, in the absence of proper reference compounds, it may provide means to identify mixed valence states. The analysis of the XANES spectra has been usually performed by fitting a model composed of a combination of several mathematical functions (Lorentzian, Gaussian, or pseudo-Voigt, to represent transitions to bound states) and arctangent functions (transitions to the continuum) to the data (Kaindl et al., 1987; Lytle et al., 1990; Takahashi et al., 2000a, 2005; Cicconi et al., 2012). XANES peak fitting has been used for decades in physic and materials sciences, especially for lanthanides compounds (Kaindl et al., 1987; Lytle et al., 1990; Bianconi et al., 1987). In Geosciences, one of the first examples was the determination of Ce^{3+}/Ce^{4+} by XANES at the Ce L_{III}-edge in ferromanganese nodules, granite and cherts (Takahashi et al., 2000a,b). The authors used Ce salts as reference compounds and performed both the linear combination of end-member spectra from trivalent and tetravalent chemicals, and the spectral fitting of the XANES region. Ce^{3+} and Ce^{4+} XANES spectra, at the L_{III}-edge, show very distinctive shape (Fig. 13.8). Trivalent compounds have a single sharp resonance peak, representing excitation into the empty *5d* band, producing a fully screened $4f^1$ *5d* state (Ce^{3+}-pyrochlore in Fig. 13.8a). Tetravalent Ce compounds (e.g., CeO_2 in Fig. 13.7a) shows at least three peaks: a small band around 5720 eV ($2p \rightarrow 4f^1$) and two strong features located at ~5730 eV and at ~5738 eV, respectively assigned to $(4f^1\ L)5d$ and $4f^0\ 5d$ configurations[2] (Kaindl, 1987; Takahashi et al., 2000a,b). According to Takahashi et al. (2000a), the sharp peak of trivalent Ce compounds can be fitted by the combination of a Lorentzian and an arctangent function, whereas in Ce^{4+} compounds, one Lorentzian function and one arctangent function are assigned to each peak. Besides, Ce^{4+} compounds show spectral shapes that depends on the chemical environment of Ce (Bianconi et al., 1987; Soldatov et al., 1994). Examples of such fits are reported in Fig. 13.8c,d. The deconvolution of spectra related to mixed valences is very challenging because of the several electronic transitions embedded in the XAS signals.

Based on the linear combination of XANES spectra for Ce^{3+} and Ce^{4+} reference materials, Takahashi et al. (2000a) estimated the Ce^{3+}/Ce^{4+} ratio in different natural materials, with an error of ~10 %. Since the shape of the Ce^{4+} XANES spectra changes depending on the element local environment, the selection of the appropriate reference compound is critical, particularly when studying silicate melts or glasses. Indeed, as previously mentioned, XAS spectra of amorphous materials present less features compared to crystalline compounds, making their interpretation even more challenging. In case of Ce, while

[2] L indicates a hole in the ligand shell

the Ce^{3+} XANES spectrum in a glass does look like that of a crystalline compound, the spectra of Ce^{4+} in glasses do not (e.g., Burnham & Berry, 2014). Thus, in order to estimate the proportions of Ce^{3+} and Ce^{4+} in glasses or melts, it is possible to linearly combine the two end-members spectra of Ce^{3+} and Ce^{4+}, acquired in the same matrix, to fit that of the sample. This linear combination method provides then a ratio that yields the Ce^{3+}/Ce^{4+} ratio in the analyzed material. This is one of the most accurate methods to determine Ce oxidation state in given materials (e.g., Takahashi et al., 2000a; Burnham & Berry, 2014). An example of this method is reported in Fig. 13.8b. In-situ dispersive XANES data were acquired on a Ce-doped sodium disilicate melt (Cicconi et al., 2017b); the trivalent and tetravalent cerium end-members were obtained at $T > 1100$ K, under oxygen fugacity conditions controlled by O_2 and Ar/H_2 gases, respectively. This approach allows an estimation of Ce redox state with higher accuracy (errors between 2 and 5 %) with respect the deconvolution method, and does not require several well-known model compounds. However, it requires the acquisition of the Ce^{3+} and Ce^{4+} signals in the same matrix, under very reduced and oxidized conditions respectively. This step can represent a challenge, making this method difficult to apply in some situations.

Advantages, drawbacks, accuracy

X-ray Absorption Spectroscopy is a powerful element-selective technique that allows studying a photoabsorber element, even at very dilute conditions, and in any physical state (crystalline, amorphous, liquids, gases). Hence, its use for either standard experiments, sample mapping, or for in-situ experiments at extreme conditions of temperature, pressure, or oxygen fugacity has increased in the last decade. XANES spectroscopy works for all transition elements (like Cu, Cr, Ti, or Eu; for example, see Berry et al., 2006a,b; Doyle et al., 2016; Burham et al., 2015) up to U for stable element (Caisso et al., 2014) and also for transuranian elements like Americium (Caisso et al., 2015; Prieur et al., 2018). Moreover, for some elements, it is also possible to acquire data at different edges. For example, several elements like Fe or V can be investigated at the K-edge (Calas and Petiau, 1983a,b; Wilke et al., 2001; Berry et al., 2010) and the L-edge (Bourdelle et al., 2013; Hoche et al., 2013).

Despite its attractiveness, XAS presents several drawbacks. The first challenge is that XAS experiments usually require the use of a synchrotron source. This typically involves the submission of a scientific proposal to large-scale facilities (synchrotron light sources), and thus it is necessary to provide a clear explanation of why it is critical to obtain data from synchrotron radiation (this statement is valid for all synchrotron-based technique), and most importantly, a prior deep knowledge of the investigated samples is required. Once access to a light source is granted, then several other things need to be carefully prepared. Particular attention to detail is required when planning an experiment as well as during data collection. The quality of the signals and the accuracy of collected data will depend on the probed photoabsorber element, as well as on its concentration.

The selection of the detection mode might be critical, because secondary effects may interfere with the signals. Examples of such unwanted effects are self-absorption or induced beam damage (i.e., see for sulfur Metrich et al., 2002, 2003, 2010; and for iron Goncalves et al., 2013, and Cottrell et al., 2018; Hughes et al. 2018, 2020). Finally, the accuracy of the experiment will depend on the standard used and on how the sample is prepared. Before performing an experiment, it is necessary to select the appropriate reference compounds. All samples should further be prepared according to the selected detection mode chosen and to the type of analyses performed (e.g., XANES vs EXAFS). Particular attention should be placed upon analyzing crystalline materials because of the dependence of the XAS features on polarization. A detailed list of practical issues on sample preparation, errors, and type of experiments is reported in Bunker (2010).

To conclude this part, we want to bring to the attention of the reader problems arising when analyzing complex samples, formed by mixtures of minerals, with possibly additional amorphous phases. For example, Fig. 13.9 represents a schematic drawing of the texture of a lava sample containing glass and crystal, from which XAS spectra at the Fe K-edge and Raman spectra were collected. Such an example is fairly representative of many natural samples, as they usually consist of a mixture of several minerals and possibly glass/amorphous phases. Depending on the beam size and of the experimental settings, it is nowadays easy to analyze small areas, typically of micron size, with a good spatial resolution and precision. Now, it seems obvious that, if the analyzed zone contains several phases, results will represent a convolution of the signals from the different phases (Fig. 13.9). It is quite difficult to find the end-members forming the analyzed mixture by numerical methods. Some studies tried to perform such calculations in order to introduce correcting terms to take into account such mixing effects, but this should be discouraged for several reasons. First, such correction implies a linear mixture of the original signals, and this may be very far from the reality due to, e.g., different refractive index and absorption coefficients of the analyzed phases that result in the beam sampling differently the different phases. Then, such correction has no physical meaning, and, as the ground for any good scientific study is the robustness of the reported data, avoiding mathematical tricks to try gathering information from discussable datasets is best practice.

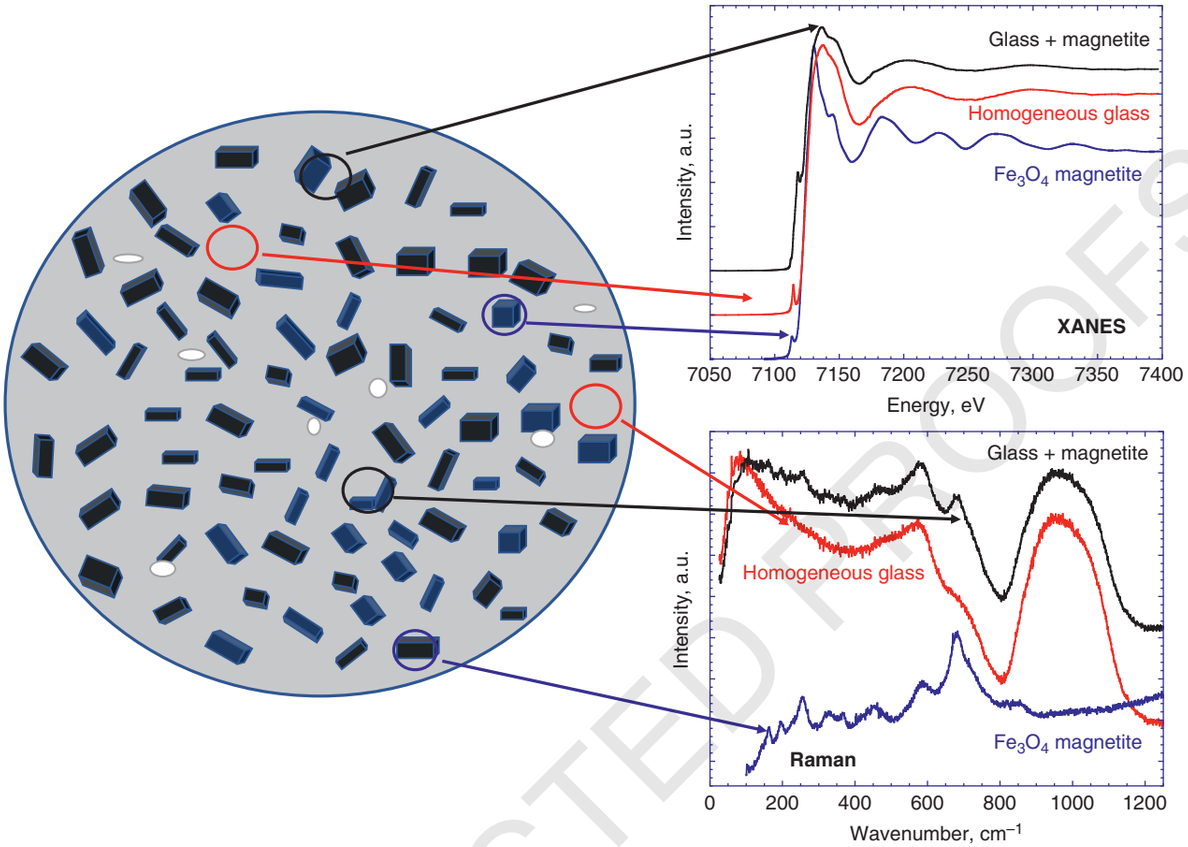

Figure 13.9 Schematic drawing of a lava, and XAS spectra at the Fe K-edge and Raman spectra of magnetite crystal, basalt glass, and their mixture. The mixed spectra are very different from the end-members in both XAS and Raman. In some cases, the end-members spectra can be used to find the proportions of the end-members, but this requires perfect knowledge of the two end-members spectra and of their mixing behavior. For example, De Ligny and Neuville (2017) have shown that it is possible to determine the rate of nucleation and growth in well-characterized, reference silicate melts from the principal component analysis of their Raman spectra acquired in situ at high temperature. However, for geologic products, such approach is very challenging because end-members spectral components as well as their mixing behavior are often unknown.

13.7. RAMAN SPECTROSCOPY

Vibrational spectroscopies, such as Raman spectroscopy, have provided information on the structure of materials in many fields. Numerous Raman studies have been carried out on silicate glasses and have made it possible, among other things, to determine the spectral treatment procedure (Mysen et al., 1982; Seifert et al., 1982), to acquire structural information on different alumino-, alkaline, and alkaline-earth silicate glasses (Mysen et al., 1980, 1981, 1985; McMillan et al., 1992; Mysen and Frantz, 1992; Neuville and Mysen, 1996; Neuville, 2006) and on iron-bearing glasses (Mysen et al., 1984, 1985; Cooney and Sharma, 1990; Wang et al., 1995; Magnien et al., 2004, 2006, 2008; Roskosz et al., 2008; Cochain et al., 2012; Di Genova et al., 2015, 2016, 2017; Le Losq et al., 2019). Despite such interest, few authors have attempted to highlight the influence of redox on Raman spectra or to perform a calibration aimed at the determination of the redox state of iron in glasses. Such analysis could benefit from the advantages of Raman spectroscopy, being a cheap, easy to access, of micrometer-scale resolution, non-destructive method that requires minimal sample preparation.

Materials, whatever their form (liquid, gas, or solid), are an arrangement of atoms linked by chemical bonds, forming molecules that can be assimilated to harmonic oscillators. Vibrational (Infrared, Brillouin, Raman) spectroscopy analyzes the excitation and the vibrations of such

molecular vibrators, following the interaction between the material and an incident electromagnetic radiation.

When a monochromatic beam passes through a transparent material, most of the incident electromagnetic beam is transmitted through the material without interacting with it. This process is an elastic scattering or Rayleigh scattering, for which the chemical bond returns to its original vibrational state. In this case, the frequency of the transmitted electromagnetic wave is that of the incident radiation. However, a tiny portion of the incident wave undergoes inelastic scattering: this is the Raman effect. The frequency of scattered radiation differs from that of the incident beam because the excited molecular vibrators did not return to its energy initial state; in other terms, they exchanged energy with the incident photons. Two inelastic scattering scenarios are possible: Raman Stokes and Raman anti-Stokes. For Stokes scattering, the photons gave energy to the vibrator that returns to a higher energy state, such that the scattered photons' vibrational frequency is less than that of the incident radiation. Conversely, in the case of the anti-Stokes scattering, the photons absorbed energy from the molecular vibrators that return to a lower energy level, and, hence, scattered photons have a higher frequency.

As a result, Raman spectra present bands that are signatures of the chemical bonds and molecular groups in a material, in two regions (Stokes and anti-Stokes) which frequencies are located symmetrically on both sides of the exciter frequency. Generally, only the Stokes part of Raman spectra is exploited. Indeed, at room temperature, anti-Stokes lines are less intense than Stokes lines because Boltzmann's statistic indicates that molecules are close to their ground states and thus are more likely to go to a higher energy state. An exhaustive review on Raman spectroscopy applied to Earth and Material Sciences was made by Neuville et al. (2014), and another one by de Ligny and Neuville (2017) on its application to the study of the crystal nucleation and growth phenomenon.

13.7.1. Spectrometer, Technical Designs, Acquisition Parameters

A Raman spectrometer generally consists of a laser source (argon or krypton), which can emit monochromatic light at several different wavelengths. The incident beam is focused on the sample through a confocal system that consists of diaphragms, lenses, and an optical microscope. The confocal system also collects and filters the backscattered beam, then transmits it to a premonochromator and spectrometer for analysis. Through a set of networks and mirrors, the beam is filtered and diffracted to arrive on a multichannel CCD detector which converts it into a spectrum I(ω), where I(ω) is the number of photons at the wavenumber ω, usually expressed in cm^{-1}. As Raman spectroscopy measures photons that present a frequency shift from those constituting the incident beam, ω should actually be referred as the Raman shift.

Currently, a large choice of spectrometers is available. Their price can vary from a few thousand euros to over two hundred thousand euros, depending on the spectral accuracy, the laser sources, and the proposed equipment such as a confocal microscope. Aside the traditional laboratory spectrometers, it also is possible now to find relatively accurate portable Raman spectrometers that allow real *in situ* analysis in the field. Such developments bring new opportunities to use Raman spectroscopy directly *in situ*, for analyzing rocks, pigments, or fragile samples for various purposes related to studies in fields like geology, archeology, volcanology, or material sciences. Such attractiveness is reinforced by forthcoming developments in the treatment of the Raman signal with using machine learning algorithms in conjunction with spectral databases. This allows automatic recognition of minerals phases for instance.

13.7.2. Raman Spectra

As previously said, Raman spectra show bands characteristic of specific chemical bonds and molecular groups. More detailed about band vibration, selection rules, molecule vibrations can be found in several books like Hersberg (1945a,b), Wilson et al.(1955), Long (1977), or Harris and Bertolucci (1978). To summarize, the length and the strength of chemical bonds vary according to the cations, their coordination numbers, as well as the strengths of the bonds involved in the molecule. As a result, Raman bands are representative of the coexisting structural units in silicate glasses and fuses, making Raman spectroscopy a powerful tool for probing the structure and state of polymerization of silicates (Brawer, 1975; Brawer & White, 1977; Furakawa & White, 1980; Mysen et al., 1980, 1981).

13.7.3. Spectral Pre-Treatment: Background Subtraction and Normalization

To obtain quantitative information from a Raman spectrum, it is necessary to (i) correct for temperature and excitration line effects; (ii) remove any remaining background; and (iii) normalize the spectra.

The measured intensity depends on the wavelength and temperature (effect of the Bose-Einstein distribution of excited phonons) of acquisition (Long, 1977). Those effects can be removed using the equation

$$I = Iobs\left[\nu o^3 \nu/(\nu o - \nu)^4\right]\left[1 - \exp\left(-hc\nu/kT\right)\right] \quad (13.9)$$

with h the Planck constant, k the Boltzmann constant, c the speed of light in m s^{-1}, T the temperature in K, νo the wavenumber of the incident laser light in m^{-1}, and ν the measured Raman shift in m^{-1}. This correction is mostly important if one wants to observed peaks at low frequency (lower than ~500 cm^{-1}; see Neuville et al., 2014). Its origin and variants can be found in Shuker and Gammon (1970), Galeener and Sen (1978), Brooker et al. (1988), and Hehlen et al. (2010). Some software offers the different variants, see the function *tlcorrection* from the *rampy* library in Python for instance.

Often spectra are affected by a background. Part of it can be removed prior to the temperature and excitation line effect correction (Equation 13.9), but some background can still persist after this correction. Spectral background can arise from many different sources, including adsorbed OH groups on sample surface, black-body radiation in high temperature experiments, and incident light scattering interference in the sample (the latter is particularly visible in multiphasic samples). To remove such background, one can either acquire a spectrum of the spectrometer and setup without the sample. This allows, for instance, the removal of the signal of diamond during diamond-cell experiments. Note that, in this case, the correction described by Equation 13.9 is applied (if applied) after the subtraction of the known background. However, such approach will not allow taking into account any effect due to the interaction between the sample and the laser. Therefore, a common practice is to use a flexible mathematical function fit to the minima in the spectra. This function represents an empirical best approximation of the true background, and after being subtracted from the raw spectrum, it allows obtaining a background corrected spectrum. Several functions can be used, like polynomial functions or splines, but the most promising developments nowadays reside in automatic methods like the ALS (Eilers and Boelens 2005) and arPLS (Baek et al., 2015) background subtraction techniques. Those methods are fairly good for Raman spectra of minerals as they present peaks very distinct from the baseline. The treatment of glass Raman spectra require more effort because minima often contain the tails of the broad peaks arising from the vibration of the disordered molecular entities composing amorphous materials. Therefore, background is often manually fit to specific areas using user-defined functions. In any case, many libraries allow one to perform background subtraction in an interactive way in many programming languages (see for instance *rampy* in Python, *hyperSpec* in R, *Baseline Fit* in Matlab/Octave, *Spectra* in Julia). As different choice of background can severely influence the obtained result, and as a manual fit using a graphical interface is often non-reproducible even by the same user, we advocate the implementation of systematic iterative computer codes for background fitting and subtraction, such that those codes can be provided to the community for their use and accuracy evaluation.

After background fitting, normalization of the intensity is often desired. Depending on the goal of the study, different choices can be made. At this stage, we should recall that Raman spectra represent a glimpse into the [KT] vibrational density of state (VDoS) [\KT] of materials. The integral of the VDoS is equal to 1 by definition, as it is that of the intensities of all the observed vibrations. Therefore, in case of doubt regarding normalization, a best practice is to simply normalize the observed intensities by their integral, i.e., the area under the Raman spectral signal. However, sometimes other choices can be made for representation purpose of easiness of analysis. For instance, it is also possible to normalize the observed intensities to that of the maximum of a given peak, or to a value measured at given Raman shift. In any case, different choices can be considered depending on the goal of the Raman analysis: (i) either treat the data to obtain information relevant to our study, so in this case we can choose any protocol as long as we stick with it; or (ii) process the spectra for comparison with the literature. In the latter case, it is necessary to use the same protocols as described in previous studies. We must conclude by stressing that, if several pieces of information are to be extracted from the same spectrum, normalization to the total area of the spectrum will be necessary. This will provide information comparable to that obtained by other techniques (NMR and XANES, cf. Cochain et al., 2012), as well as volatile content (Le Losq et al., 2012).

13.7.4. Details on Raman Spectra of Silicate Glasses

Fig. 13.10 show a normalized Raman spectrum of pyroxene glass composition (50 mol% SiO_2 – 5 mol% Na_2O – 22.5 mol% MgO – 22.5 mol% CaO). This spectrum is composed by several frequency regions: (i) a low frequency region at Raman shifts < ~600 cm^{-1}; (ii) an intermediate region comprised between ~600 and ~800 cm^{-1}; (iii) a high frequency region between ~800 and ~1200 cm^{-1}. More detail can be found in Neuville et al. (2014). The bands observed were associated with the modes of vibration and various silicate structural units (Mysen et al., 1980; McMillan, 1981; McMillan et al., 1982).

The bands composing the spectra of amorphous silicates are relatively broad and unresolved compared to those of the crystals. The width of the bands results from the disorder of the amorphous structure, marked for instance by the large pseudo-Gaussian distributions of bonding forces and angles inherited from the Brownian motions of ionic entities at high temperature in the liquid state (Mysen et al., 1982), from which the glasses were

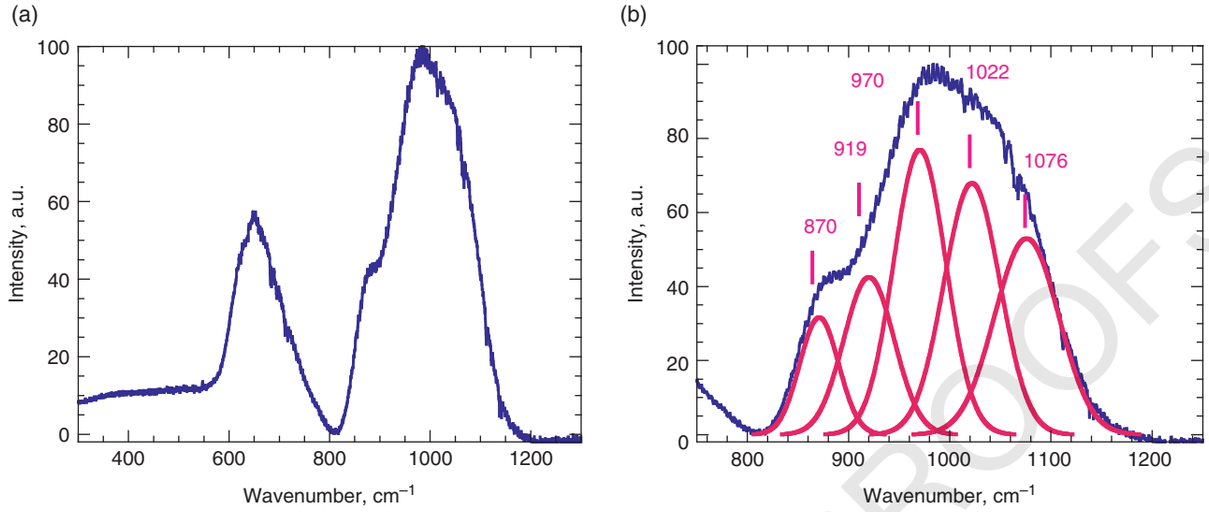

Figure 13.10 Raman spectrum of an iron-free pyroxene glass ($CaO\text{-}SiO_2\text{-}Na_2O\text{-}MgO$) at room temperature. (a) Standardized whole spectrum (b) high-frequency envelope to highlight Q species. The 870 cm^{-1} band can be attributed to Q^1 species, 919 cm^{-1} to Q^2, 970 cm^{-1} to T_{2s}, 1022 cm^{-1} to Q^3 species, and 1076 cm^{-1} to Q^4 species (based on Magnien et al., 2006).

formed and are an image of, as well as to replacement of Si by other tetrahedral cations and to the variety of modifying cations (Brawer, 1975).

In any solid, the number of vibrational modes and the density of states are complex functions of the frequency. Generally, the analogy between a spring and the chemical bonds leads to the application of the Hooke relation:

$$\nu = \tfrac{1}{2}\,\pi * (k/\mu)^{1/2}. \qquad (13.10)$$

with ν the vibration frequency in Hz, μ the mass of the atoms involved in the bond in kg, and k the binding force in $N.m^{-1}$. In a silicate, the lattice vibrations involve a large number of atoms and are mainly stretching and bending vibrations of the M-O bonds accompanied by the movement of the TO_4 tetrahedra (M: modifying or charge compensator cations, and T network formers). Therefore, Raman bands and their frequencies are highly dependent on the state of polymerization of the network. In addition, band shape will depend on the competition between the lifetime of the virtual excited state and the coherence lifetime. Depending on such lifetime effects, bands tend to be either Gaussian, or Lorentzian, or a mixture of both. In a silicate crystal, bands usually tend to be Lorentzian while in glasses, the large bands actually tend to a Gaussian lineshape reflecting the inherent Brownian disorder of the structure of the liquids they mirror. Network modifying cations have large masses and generate weak links (high μ, low k). The frequency region at Raman shifts < 600 cm^{-1} represents the stretching vibration modes of the M-O bonds. With smaller masses and larger force constants, the vibrations associated with tetrahedral cations are localized at a higher frequency. The bands between 600 and 800 cm^{-1} are due to the bending vibrations of the O-T-O bonds and the TO_4 tetrahedra, more particularly to the Si movement in its tetrahedral cage accompanied by a slight movement of the oxygen atoms. Their intensity and frequency decrease with increasing polymerization (Sharma et al., 1984; McMillan, 1994). Finally, the high frequency bands in the 800–1200 cm^{-1} envelope represent the symmetric stretching vibrations of the T-O-T bonds. Their intensity and frequency increase with increasing polymerization (Mysen et al., 1980; McMillan, 1984).

The bending and stretching vibration are essentially in two frequency domains 500–700 cm^{-1} and 800–1200 cm^{-1} and are strongly correlated with the various tetrahedral Q species and thus with non-bridging oxygens (Q^n, where n = number of bridging oxygens) (Mysen et al., 1980; McMillan, 1984). In particular, the relatively high-frequency envelope has several contributions. As a result, it has undergone numerous deconvolution and modeling treatments to determine the number, position, and intensity of contributions for various glass compositions (Mysen et al., 1980, 1981; Seifert et al., 1982, among others). Since Mysen et al., (1980), it is commonly accepted that:

- Q^0 species (SiO_4^{4-}) are between 850 and 880 cm^{-1};
- Q^1 ($Si_2O_7^{6-}$) between 900 and 920 cm^{-1};
- Q^2 ($Si_2O_6^{4-}$) between 950 and 980 cm^{-1};
- Q^3 ($Si_2O_5^{2-}$) between 1050 and 1100 cm^{-1};

• Q^4 (SiO_2) between 1060 and 1190 cm^{-1}.

Furthermore, another band is generally used, called T_{2s}, between 950 and 1050 cm^{-1}, and corresponds to a stretching vibrational mode of TO_4 tetrahedra (see details in Le Losq et al., 2014). Fig. 13.10a,b shows a spectrum of an iron-free silicate glass composition and the deconvolution into five tetrahedral units of the high-frequency envelope.

Raman studies have shown that, in alkali and alkaline-earth silicate glasses, the abundances of the Q species are linked by the disproportionation reactions:

$$2\,Q^n \Leftrightarrow Q^{n+1} + Q^{n-1}, \qquad (13.11)$$

with $4 > n > 0$. The equilibrium constants of those reactions depend on temperature, aluminium concentration as well as the mean ionic field strength of the non-network former cations. More details can be found in, e.g., Mysen (1988, 1990, 1996) and Mysen et al. (2003).

13.7.5. Raman Spectra of Iron Silicate Glass

Silicate compositions containing iron have been studied by Raman spectroscopy, mainly to interpret the structural role of iron and to try to link the achieved redox equilibrium to the silicate glass/melt structure (Mysen et al., 1980, 1984; Fox et al., 1982; Cooney & Sharma, 1990; Wang et al, 1995). More recently, studies also focused on the determination of Fe redox ratio in glasses from their Raman spectra (Magnien et al., 2006; Roskosz et al., 2008; Di Muro et al., 2009; Cochain et al., 2012; Neuville et al., 2014a; Di Genova et al., 2016; Le Losq et al., 2019). The vibrations of the bonds depending on the substitution of silicon by other forming cations (Fe^{3+} in particular), the Raman bands, and in particular the high-frequency envelope can be considered as tools for characterizing the structural role of iron.

Magnien et al. (2006) performed an analysis of spectra of iron-pyroxene glasses (Fig. 13.11), revealing that the intensity of bands at ~910 and ~550 cm^{-1} increases with increasing the oxidation of those glasses from 0.09 to 0.99. Despite clear changes, the analysis of Raman spectra with the redox state remained purely qualitative in this study. It corroborated results from earlier works (Mysen et al., 1980; Virgo et al., 1983; Wang et al., 1995) that showed that Fe^{3+}-O stretching vibrations give rise to a signal between 900 and 990 cm^{-1} in Raman spectra of iron-bearing silicate and aluminosilicate glasses. Fe^{2+} in the octahedral position does not yield any signal, or possibly at low frequencies (< 500 cm^{-1}) mixed with stronger signals from T-O-T bonds in silicate glasses.

Fig. 13.12 a,b show Raman decompositions of the 0.09 and 0.99 spectra shown in the previous figure. The intensity of the 910 cm^{-1} band increases clearly with the Fe^{3+} content in the iron-pyroxene glass. This 910 cm^{-1} band

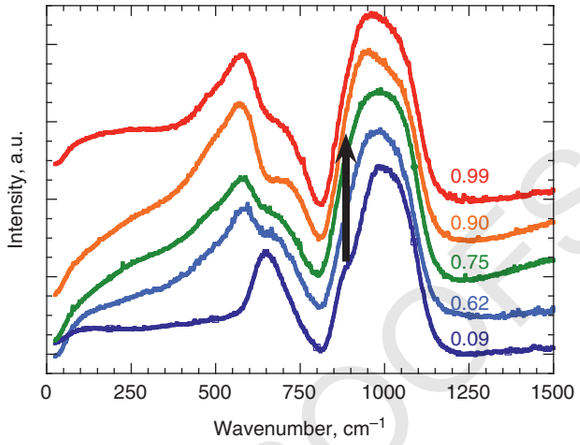

Figure 13.11 Raman spectra at room temperature for a series of iron-pyroxene glasses. The Fe^{3+}/Fe^{tot} redox ratio is indicated to the right of the spectra and the curves have been shifted to facilitate the observation of the changes. These spectra were normalized at the maximum intensity of the spectra corrected from the excitation lines (see Neuville et al., 2014). Figure adapted from Magnien et al., 2006.

shifts in frequency as a function of the chemical composition of the glass. As a consequence, in aluminosilicates, borosilicates, or highly polymerized compositions, this band will be rather be located around 990 cm^{-1}. In borates, this band is around 1300 cm^{-1} whereas in aluminates it is at 650 cm^{-1} (El Hayek, 2016). In any case, in silicate glasses, this Raman band at ~ 910 cm^{-1} correlates perfectly with the variations of the Fe pre-edge peak observed in Fe K-edge XANES spectra.

As a result, it is possible to calibrate the variations of intensity of this peak with the iron redox state in the glass. For instance, the iron-pyroxene glass was investigated by Magnien et al. (2004, 2006, 2008) with different techniques, like Mössbauer spectroscopy, wet chemical analyses, XANES at the Fe K-edge, and Raman spectroscopy. The comparison of all these techniques are plotted in Fig. 13.13 and show a good agreement of the Fe redox states measured by the different techniques. However, it should be remembered that XANES and wet-chemical analyses are absolute measurements, whereas electronic microprobe and Raman spectroscopy need calibrations.

The measurement of the iron redox ratio by Raman spectrometry is based on the use of a set of the Raman spectra of glass standards with known redox ratio, and the establishment of a calibration linking changes in the spectra to variations in the glasses' iron redox ratios. After acquisition, several methods can be used:

• calibrate the changes in intensity of the peak around 910 cm^{-1} to the iron redox state in the glass (Magnien et al., 2006; Roskosz et al., 2008; Le Losq et al., 2019);

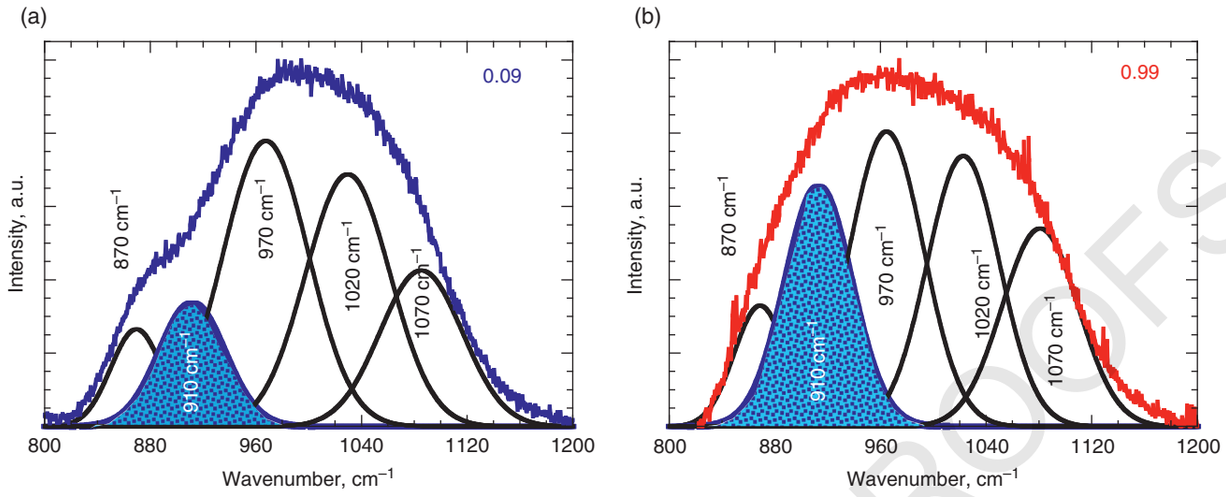

Figure 13.12 a,b: Deconvolution of the 0.09 and 0.99 Raman spectra (based on Magnien et al., 2006).

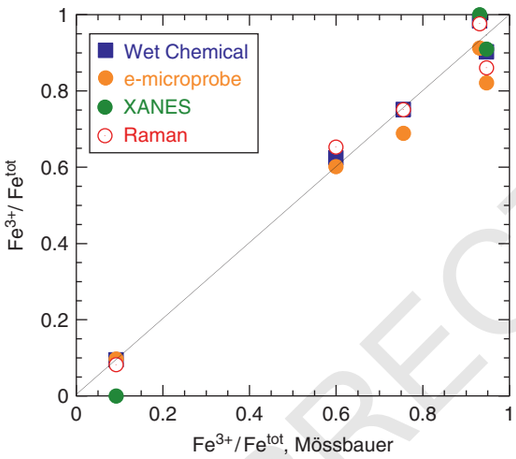

Figure 13.13 Comparison of iron ratios analyzed by different techniques, wet chemical, e-microprobe, XANES at the Fe K-edge, and Raman spectroscopy (redrafted from Magnien et al., 2004, 2006).

• use a linear mixture of end-member spectra (Di Genova et al., 2016);
• peak-fitting (Di Muro et al., 2009; Welsh et al., 2017);
• machine learning methods (Le Losq et al., 2019).

Le Losq et al. (2019) recently compared the use of six methods (intensity, linear mixture, and machine learning algorithms like neural networks or support vector machines) on a set of basalt glass standards synthesized in the lab at well know oxygen fugacity conditions, and analyzed by Mossbauer spectroscopy. They demonstrated that, on a given glass composition, an accuracy of 0.02 Fe^{3+}/Fe^{tot} can be reached with Raman spectroscopy. However, they also showed that, as small changes in glass compositions affect quite strongly the glass structure and, hence, Raman spectra, Fe redox Raman determination is very sensitive to matrix effects. With using a correction for this effect, they were able to measure the redox state of mid-ocean ridge basalts at 0.09 ± 0.06 Fe^{3+}/Fe^{TOT}.

Advantages, drawbacks, accuracy

Raman spectroscopy benefits from several advantages:
• micrometric resolution, allowing mapping and precise spatial measurements;
• non-destructive (but… see below);
• good precision can be achieve with simple technique like following the intensity of a peak (down to 0.02 Fe^{3+}/Fe^{TOT});
• possibility of in situ experiments, at high temperature and high pressure or directly in the field with a portable Raman spectrometer.

However, several drawbacks also affect this method:
• it is a relative method, requiring glass standards…
• … and chemical effects are strong as Raman spectra are a picture of the entire vibrational landscape of the samples;
• at elevated laser power, beam damage can be a problem (e.g., see Di Genova et al., 2017), but this can be avoided with the use of filters to decrease laser power;
• consistent, systematic data treatment protocol are necessary to obtain reproducible results; consequently, data processing via computer programming is strongly advised (spectrum-by-spectrum hand treatment should be avoided at all cost);
• strong sensitivity to the structure, hence composition of glasses, such that changes in major element composition and redox-related changes are mixed and difficult to desantangle;
• fluorescence and luminescence are often important problems when analyzing natural samples;
• it is rare to have pure glasses in natural samples, free from any crystals even nanolites, making the use of Raman challenging as soon as crystal peaks are detected.

In the future, it may be possible to study other pairs of redox than Fe^{3+}/Fe^{tot} in glasses, but for the moment it is the only redox couple well characterized. However, couples such as Ce^{4+}/Ce^{3+} may be considered. Such study requires that the two elements be in different roles depending on their redox, network former or network modifier. A priori Raman spectroscopy should not work to study Cr redox as Cr structural role in silicate glass is independent of its redox. One may note that Raman spectrometry can also be used to investigate redox volatile elements as recently demonstrated by Cicconi et al. (2019a,b) for the study of iodine dissolved in vitreous silicate.

13.8. IN SITU REDOX DETERMINATION AT HIGH TEMPERATURE OR AT HIGH PRESSURE

Recently Mössbauer spectroscopy was used at high pressure to measure the redox state in a diamond anvil cell at 100 GPa. This experiment is very fast, around 10 minutes, whereas such an experiment with a radioactive point source would take more than one week and the data quality would be considerably less (Potapkin et al., 2012). These new technical developments carried out at the ESRF are very promising and should allow in the coming years to better answer the questions of redox of the mantle phases, and more generally to improve the knowledge of redox equilibria at high pressure.

High temperature experiment: several setups were developed to conduct high-temperature experiment to investigate redox state: a HT furnace to made XANES (Berry et al., 2003b); the levitation device (Alderman et al., 2017), and the micro heating device originally developed by Mysen and Frantz (1992) and modify to use for XANES, WAXS, IR, Raman spectroscopies (Neuville, et al, 2014b).

In the next part, two examples will be shown using a micro heating device to measure Raman spectroscopy and XANES at the Fe K-edge on the same pyroxene (50%SiO_2–5%Na_2O–20% MgO–20%CaO-5%FeO) composition at high temperature (Fig. 13.14).

Fe^{3+}/Fe_{Tot} redox ratio plotted in Fig. 13.15 is calculated from the XANES treatment of the pre-edge and Raman deconvolution following procedure given in

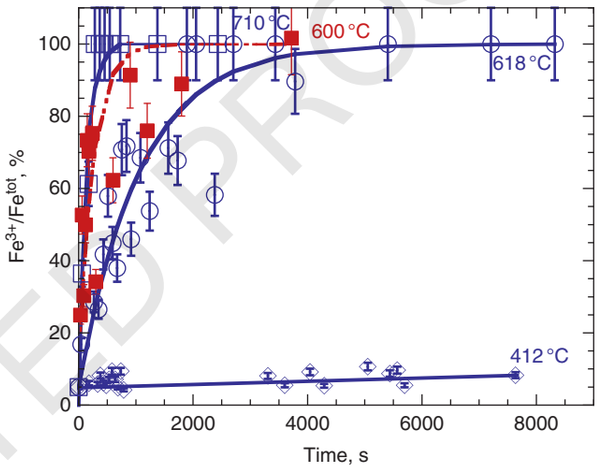

Figure 13.15 Fe^{3+}/Fe_{Tot} redox as different temperatures, 412, 618, 710 °C from XANES measurements at the Fe K-edge and at 600 °C from Raman spectroscopy (redrafted from Magnien et al., 2006, 2008).

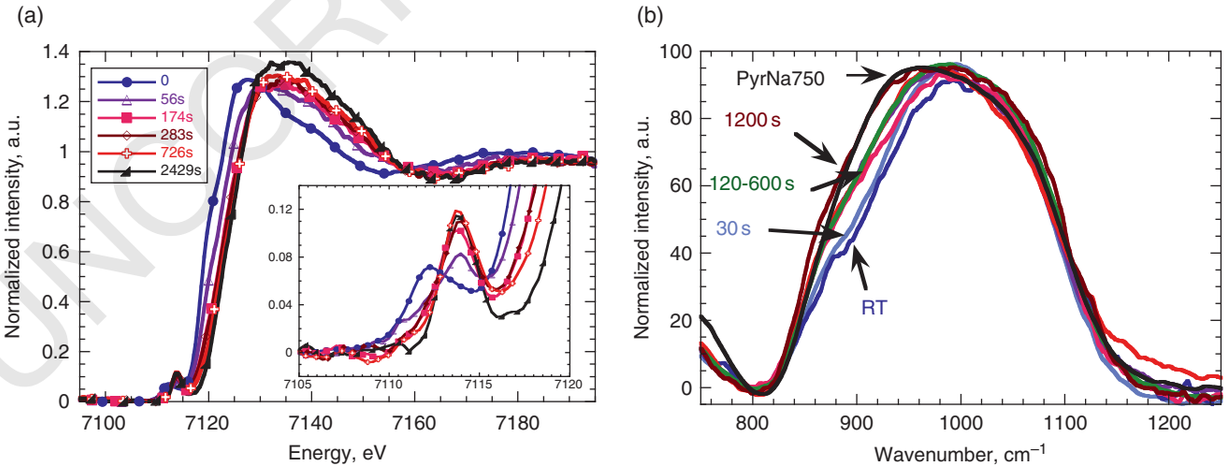

Figure 13.14 (a) Evolution of the normalized XANES spectra at the Fe K-edge and a zoom on the associated pre-edge of PyrNa17R at 710 °C (T g + 100 °C) as a function of time. The times are indicated in the legend. (b) Raman spectra as a function of time for PyrNa17R at 600 °C (redrafted from Magnien, 2005).

Table 13.2 Summarize of analytical techniques and their advantages.

	Wet chemical	Electron microprobe	Mossbauer	XANES	Optical absorption	Raman
All elements	X			X	X	
Specific		Fe	Fe, Sb, I, Ni…			Fe
Destructive	X	X	X	X	X	
Not preparation						X
Short preparation	X	X				
Long preparation			X	X	X	
Easy access	X	X			X	X
Request access			X	X		

Sections 13.6 and 13.7 or more detailed in Magnien et al. (2006, 2008).

The variation of redox ratio as a function of time at different temperature observed by Raman spectroscopy and by XANES at the Fe K-edge show similar variation, which proves a good agreement between the two techniques.

From this redox variation at high temperature observed by Raman spectroscopy or XANES at the Fe K-edge it is possible to determine redox diffusion coefficient as shown by Magnien et al. (2008), for example. This was also recently used by Le Losq et al. (2020) to follow redox disequilibrium at high temperature on the andesite of Erebus volcanoes.

13.9. CONCLUSION

In this chapter, we briefly reviewed six techniques that allow the quantification of the oxidation state of an element in different samples (mineral, glasses, rocks) and in different physical states (solid, melts). Each method presents different advantages and drawbacks. Some will be suited for absolute measurements like wet chemistry, while others require standards but may allow mapping (electron microprobe or Raman spectroscopy). Table 13.2 summarize the six techniques and their advantages and access.

Future developments in term of technique, like synchrotron Mössbauer, or data treatment with, in particular, machine learning, may allow pushing further the boundaries of possibilities and seeking more and more information from experiments and naturals samples. Raman spectroscopy and XANES at the different M, L, or K-edge can be also measured directly at high temperature which can provide the possibility to measure and follow redox kinetics of melts directly at high temperature (Magnien et al., 2008; Neuville et al., 2014; Prieur et al., 2018; Caisso et al., 2017).

Acknowledgments: MRC thanks the Naturhistorische Gesellschaft Nürnberg, Prof. Dr. Mischka and Ms. Horlacher for the archeological glass.

REFERENCES

Abe, H., Aquilanti, G., Boada, R., Bunker, B., Glatzel, P., Nachtegaal, M., & Pascarelli, S. (2018). Improving the quality of XAFS data. *Journal of Synchrotron Radiation*, *25*(Pt 4), 972–980. doi:10.1107/S1600577518006021

Albee, A. L., & Chodos, A. A. (1970). Semiquantitative electron microprobe determination of Fe 2+/Fe 3+ and Mn2+/Mn3+ in oxides and silicates and its application to petrologic problems. *American Mineralogist*, *55*, 491–501.

Alderman O., Wilding M. C., Tamalonis A., Sendelbach S., Heald S. M., Benmore C. J., et al. (2017). Iron K-edge X-ray absorption near-edge structure spectroscopy of aerodynamically levitated silicate melts and glasses. *Chemical Geology*, *453*, 169–85. doi: 10.1016/j.chemgeo.2017.01.020

Baek S.-J., Park A., Ahn Y.-J., & Choo J. (2015) Baseline correction using asymmetrically reweighted penalized least squares smoothing. *Analyst*, *140*, 250–257. doi: 10.1039/C4AN01061B

Bajt S., Sutton S. R., & Delaney J. S. (1994). X-ray microprobe analysis of iron oxidation states in silicates and oxides using X-ray absorption near edge structure (XANES). *Geochimica et Cosmoschimica Acta*, *58*, 5209–5214. https://doi.org/10.1016/0016-7037(94)90305-0

Bancroft, M., Nesbitt, H. W., Henderson, G. S., O'Shaughnessy, C., Withers, A. C., & Neuville, D. R. (2018). Lorentzian dominated lineshapes and linewidths for Raman symmetric stretch peaks (800–1200 cm−1) in Qn (n=1–3) species of alkali silicate glasses/melts. *Journal of Non-Crystalline Solids. 484*, 72–83. https://doi.org/10.1016/j.jnoncrysol.2018.01.018

Berry A. J., & O'Neill H.St.C. (2004). A XANES determination of the oxidation state of chromium in silicate glasses. *American Mineralogist*, *89*, 790–798. https://doi.org/10.2138/am-2004-5-613

Berry, A. J., O'Neill, H.St.C., Jayasuriya, K. D., Campbell, S. J., & Foran, G. J. (2003a). XANES calibration for the oxidation state of iron in a silicate glass. *American Mineralogist*, *88*, 967–977. https://doi.org/10.2138/am-2003-0704

Berry, A. J., Shelley, J. M. G., Foran, G. J., O'Neill, H.St.C., & Scott, D. R. (2003b). A furnace design for XANES spectroscopy of silicate melts under controlled oxygen fugacities and temperatures to 1773 K. *Journal of Synchrotron Radiation*, *10*, 332–336. 10.1107/s0909049503007556

Berry, A., O'Neill, H.St.C., Scott, D. R., Foran, G. J., & Shelley, J. M. G. (2006a). The effect of composition on Cr 2+ /Cr 3+ in silicate melts. *American Mineralogist*, *91*, 1901–1908. https://doi.org/10.2138/am.2006.2097

Berry, A., Hack, A. C., Mavrogenes, J. A., Newville, M., & Sutton, S. R. (2006b). A XANES study of Cu speciation in high-temperature brines using synthetic fluid inclusions. *American Mineralogist*, *91*, 1773–1782. https://doi.org/10.2138/am.2006.1940

Berry, A. J., Yaxley, G. M., Woodland, A. B., & Foran, G. J. (2010). A XANES calibration for determining the oxidation state of iron in mantle garnet. *Chemical Geology*, *278*, 31–37. https://doi.org/10.1016/j.chemgeo.2010.08.019

Berry, A. J., Stewart, G. A., O'Neill, H.St.C., Mallmann, G., & Mosselmans, J. F. W. (2018). A re-assessment of the oxidation state of iron in MORB glasses. *Earth and Planetary Science Letters*, *483*, 114–123. https://doi.org/10.1016/j.epsl.2017.11.032

Bianconi, A., Marcelli, A., Dexpert, H., Karnatak, R., Kotani, A., Jo, T., & Petiau, J. (1987). Specific intermediate-valence state of insulating 4*f* compounds detected by L3 x-ray absorption. *Physical Review B*, *35*, 806–812. doi: 10.1103/physrevb.35.806

Bingham, P. A., Parker, J. M., Searle, T., Williams, J. M., & Smith, I. (2002). Novel structural behaviour of iron in alkali-alkaline-earth-silica glasses. *Comptes Rendus Chimie*, *5*, 787–796. https://doi.org/10.1016/S1631-0748(02)01444-3

Bourdelle, F., Benzerara, K., Beyssac, O., Cosmidis, J., Neuville, D. R., Brown, G. E., Jr, & Paineau, E. (2013). Quantification of the ferric/ferrous iron ratio in silicates by scanning transmission X-ray microscopy at the Fe L2,3 edges. *Contribution to Mineralogy and Petrology*, *166*, 423–434. https://doi.org/10.1007/s00410-013-0883-4

Burnham, A. J. Berry, Halse, H. R., Schofield, P. F., Cibin, G., & and Mosselmans, J. F. W. (2015). The oxidation state of europium in silicate melts as a function of oxygen fugacity, composition and temperature. *Chemical Geology*, *411*, 248–259. https://doi.org/10.1016/j.chemgeo.2015.07.002

Brawer, S. (1975). Theory of the vibrational spectra of some network and molecular glasses. *Physical Review B*, *11*, 3173–3194. https://doi.org/10.1103/PhysRevB.11.3173

Brawer, S., & White, W. B. (1977). Raman spectroscopic investigation of the structure of silicate glasses (II). Soda-alkaline earth-alumina ternary and quaternary glasses. *Journal of Non-Crystalline Solids*, *23*, 261–278. https://doi.org/10.1016/0022-3093(77)90009-6

Brown, G. E., Calas, G., Waychunas, G. A., & Petiau, J. (1988). X-ray absorption spectroscopy; applications in mineralogy and geochemistry. *Reviews in Mineralogy and Geochemistry*, *18*, 1, 431–512.

Bunker, G. (2010). *Introduction to XAFS: A Practical Guide to X-ray Absorption Fine Structure Spectroscopy*. Cambridge: Cambridge University Press.

Burnham, A. D. D., & Berry, A. J. (2014). The effect of oxygen fugacity, melt composition, temperature and pressure on the oxidation state of cerium in silicate melts. *Chemical Geology*, *366*, 52–60. https://doi.org/10.1016/j.chemgeo.2013.12.015

Caisso, M., Lebreton, F., Horlait, D., Picart, S., Martin, P. M., Bès, R., et al. (2014). Nanostructured gadolinium-doped ceria microsphere synthesis from ion exchange resin: Multi-scale in-situ studies of solid solution formation. *Journal of Solid State Chemistry*, *218*, 155–163. https://doi.org/10.1016/j.jssc.2014.06.028

Caisso, M., Picart, S., Belin, R., Lebreton, F., Martin, P. Dardenne, K., et al. (2015). In-situ characterization of uranium and americium solid solution formation for CRMP process: first combination of in-situ XRD and XANES measurements. *Dalton Transactions*, *44*, 6391–6399. https://doi.org/10.1039/C4DT03515A

Calas G., & Petiau, J. (1983a). Structure of oxides glasses. Spectroscopic studies of local order and crystallochemistry. Geochemical implications. *Bulletin de Mineralogie*, *106*, 33–55.

Calas, G., & Petiau, J. (1983b). Coordination of iron in oxide glasses through high resolution K-edge spectra: information from pre-edge. *Solid State Communications*, *48*, 625–629. https://doi.org/10.1016/0038-1098(83)90530-6

Cerantola, V., Bykova, E., Kupenko, I., Merlini, M., Ismailova, L., et al. (2017). Stability of iron-bearing carbonates in the deep Earth's interior. *Nature Communications*, *8*, 15960. doi: 10.1038/ncomms15960

Cicconi, M. R. R., Giuli, G., Paris, E., Ertel-Ingrisch, W., Ulmer, P., & Dingwell, D. B. (2012). Europium oxidation state and local structure in silicate glasses. *American Mineralogist*, *97*(5–6), 918–929. https://doi.org/10.2138/am.2012.4041

Cicconi, M. R., Giuli, G., Ertel-Ingrisch, W., Paris, E., & Dingwell, D. B. (2015a). The effect of the [Na/(Na+K)] ratio on Fe speciation in phonolitic glasses. *American Mineralogist*, *100* (7), 1610–1619. https://doi.org/10.2138/am-2015-5155

Cicconi, M. R., Neuville, D. R., Tannou, I., Baudelet, F., Floury, P., Paris, E., & Giuli, G. (2015b). Competition between two redox states in silicate melts: an in-situ experiment at the Fe K-edge and Eu L3-edge. *American Mineralogist. 100*, 1013–1016. https://doi.org/10.2138/am-2015-5172

Cicconi, M. R., Veber, A., de Ligny, D., Rocherullé, J., Lebullenger, R., & Tessier, F. (2017a). Chemical tunability of europium emission in phosphate glasses. *Journal of Luminescence*, *183*, 53–61. https://doi.org/10.1016/j.jlumin.2016.11.019

Cicconi, M. R., Neuville, D. R., Blanc, W., Lupi, J.-F., Vermillac, M., & de Ligny, D. (2017b). Cerium/aluminum correlation in aluminosilicate glasses and optical silica fiber preforms. *Journal of Non-Crystalline Solids*, *475*, 85–95. doi:10.1016/j.jnoncrysol.2017.08.035

Cicconi, M. R., Pili, E., Grousset, L., & Neuville, D. R. (2019a). The Influence of Glass Composition on Iodine Solubility. MRS Advances. pp. 1–9 https://doi.org/10.1557/adv.2018.665

Cicconi, M. R., Pili, E., Grousset, L., Florian, P. Bouillard, J. C., Vantelon, D., & Neuville, D.R. (2019b). Iodine dissolution and speciation in glasses. *Scientific Report.* https://doi.org/10.1038/s41598-019-44274-4

Cicconi, M. R., Lu, Z., Uesbeck, T., van Wüllen, L., Brauer, D. S., & de Ligny, D. (2020). Influence of Vanadium on optical and mechanical properties of aluminosilicate glasses. *Frontiers in Materials.* https://doi.org/10.3389/fmats.2020.00161

Charlot, G. (1969). *Methods of Analytical Chemistry. Quantitative Analysis of Inorganic Compounds*. 2nd Edition, Chem., Moscow, 668pp.

Cochain, B., Neuville, D. R., de Ligny, D., Roux, J., Baudelet, F., Strukelj, E., & Richet, P. (2009). Kinetics of iron redox reaction in silicate melts: A high-temperature Xanes study on an alkali basalt. *Journal of Physics: IV*, *190*, 12182–12186.

Cochain, B., Neuville, D. R., Henderson, G. S., McCammon, C., Pinet, O., & Richet, P. (2012). Iron content, redox state and structure of sodium borosilicate glasses: A Raman, Mössbauer and boron K-edge XANES spectroscopy study. *Journal of the American Ceramics Society*, *94*, 1–12. https://doi.org/10.1111/j.1551-2916.2011.05020.x

Cook, G.B., & Cooper, R.F. (2000). Iron concentration and the physical processes of dynamic oxidation in alkaline earth aluminosilicate glass. *American Mineralogist*, *85*, 397–406. https://doi.org/10.2138/am-2000-0401

Cook, G. B., Cooper, R. F., & Wu, T. (1990). Chemical diffusion and crystalline nucleation during oxidation of ferrous iron-bearing magnesium aluminosilicate glass. *Journal of Non-Crystalline Solids*, *120*, 207–222. https://doi.org/10.1016/0022-3093(90)90205-Z

Cooney, T. F., & Sharma, S. K. (1990). Structure of glasses in the systems Mg2SiO4-Fe2SiO4, Mn2SiO4-Fe2SiO4, Mg2SiO4-CaMgSiO4 and Mn2SiO4-CaMnSiO4. *Journal of Non-Crystalline Solids*, *122*, 10–32. https://doi.org/10.1016/0022-3093(90)90220-G

Cooper, R. F., Fanselow, J. B., & Poker, D. B. (1996). The mechanism of oxidation of a basaltic glass: chemical diffusion of network-modifying cations. *Geochimica et Cosmochimica Acta*, *60*, 17, 3253–3265. https://doi.org/10.1016/0016-7037(96)00160-3

Cooper, R. F., Fanselow, J. B., Weber, J. K. R., Merkley, D. R., & Poker, D. B. (1996). Dynamics of oxidation of a Fe2+-bearing aluminosilicate (basaltic) melt. *Science*, *274*, 1173–1176. doi: 10.1126/science.274.5290.1173

Cottrell, E., Lanzirotti, A., Mysen, B. O., Birner, S., Kelley, K. A., Botcharnikov, R., et al. (2018). A Mössbauer-based XANES calibration for hydrous basalt glasses reveals radiation-induced oxidation of Fe. *American Mineralogist*, *103*, 489–501. https://doi.org/10.2138/am-2018-6268

de Groot, F. M. F., Vankó, G., & Glatzel, P. (2009). The 1s x-ray absorption pre-edge structures in transition metal oxides. *Journal of Physics: Condensed Matter*, *21*, 10, 104207. https://doi.org/10.1088/0953-8984/21/10/104207

de Ligny, D., & Möncke, D. (2019). Colors in Glasses. Chapter 9 In: *Springer Handbook of Glass*. Musgraves, J. D., Hu, J., Calvez, L. (Eds). doi: 10.1007/978-3-319-93728-1

de Ligny, D., & Neuville, D. R. (2017). Raman spectroscopy: a nice tools to understand nucleation and growth mechanism. In: From glass to crystal: nucleation, growth and phase separation, from research to applications. Neuville, D. R., Cormier, L., Caurant, D., & Montagne, L. (Eds.) EDP-Sciences.

Di Genova, D., Morgavi, D., Hess, K.-U., Neuville, D. R., Borovkov, N., Perugini D., & Dingwell, D. B. (2015). Approximate chemical analysis of volcanic glasses using Raman spectroscopy. *Journal of Raman Spectroscopy.* doi: 10.1002/jrs.4751

Di Genova, D., Kolzenburg, S., Vona, A., Chevrel, M. A., Hess, K.-U., Neuville, D. R., et al. (2016) Raman spectra of Martian glass analogues: a tool to approximate their chemical composition. *Journal of Geophysical Research Planet*, *121*, 740–752. https://doi.org/10.1002/2016JE005010

Di Genova, D., Borovkov, N., Vasseur, J., Hess, K.-U., Neuville, D. R., & Dingwell, D. B. (2017). Structure, glass transition and viscosity of alkali- and iron-rich glasses and melts with different oxygen fugacity. *Journal of Non-Crystalline Solids*, *470*, 78–85. doi: 10.1016/j.jnoncrysol.2017.05.013

Doyle, P. M., Berry, A. J., Schofield, P. F., & Mosselmans, J. F. W. (2016). The effect of site geometry, Ti content and Ti oxidation state on the Ti K-edge XANES spectrum of synthetic hibonite. *Geochimica et Cosmochimica Acta*, *187*, 294–310. https://doi.org/10.1016/j.gca.2016.05.001

Dyar, M. D., Gunter, M. E., & Tasa, D. (2008). *Mineralogy and optical mineralogy* (p. 708). Chantilly, VA: Mineralogical Society of America.

Farges, F. (2005). Ab initio and experimental pre-edge investigations of the Mn K -edge XANES in oxide-type materials. *Physical Review B*, *71*, 15, 155109. https://doi.org/10.1103/PhysRevB.71.155109

Farges F., Lefrère Y., Rossano, S., Berthereau, A., Calas, G., & Brown, Jr., G. E. (2004). The effect of redox state on the local structural environment of iron in silicate glasses: a combined XAFS spectroscopy, molecular dynamics and bond valence study. *Journal of Non-Crystalline Solids*, *344*, 176–188. https://doi.org/10.1016/j.jnoncrysol.2004.07.050

Fialin, M., Bezos, A., Wagner, C., Magnien, V., & Humler, E. (2004). Quantitative electron microprobe analysis of Fe3+/ΣFe: Basic concepts and experimental protocol for glasses. *American Mineralogist*, *89*, 654–662. https://doi.org/10.2138/am-2004-0421

Fialin, M., Wagner, C., Metrich, N., Humler, E., Galoisy, L., & Bezos, A. (2001). Fe3+/ ΣFe vs. FeLα peak energy for minerals and glasses: recent advances with the electron microprobe. *American Mineralogist*, *86*, 456–465. https://doi.org/10.2138/am-2001-0409

Fisher, D. W. (1965). Change in the soft x-ray L emission spectra with oxidation of the first series transition metals. *Journal of Applied Physics*, *36*, 2048–2053. https://doi.org/10.1063/1.1714400

Fox, K. E., Furakawa, Y., & White, W. B. (1982). Transition metals ions in silicate melts. Part 2. Iron in sodium silicate glasses. *Physics and Chemistry of Glasses*, *23*, 169–178.

Fudali F. (1965). Oxygen fugacity of basaltic and andesitic magmas. *Geochimica et Cosmochimica Acta*, *29*, 1063–1075. https://doi.org/10.1016/0016-7037(65)90103-1

Fukumi, K., Hayakawa J., & Komiyama, T. (1990). Intensity of raman band in silicate glasses. *Journal of Non-Crystalline Solids*, *119*, 297–302. https://doi.org/10.1016/0022-3093(90)90302-3

Furakawa, T., & White, W. B. (1980). Vibrational spectra and glass structure. *Journal of Non-Crystalline Solids*, *38*/39, 87–92. https://doi.org/10.1016/0022-3093(80)90399-3

Gaborieau, M., Laubier, M., Bolfan-Casanova, N., McCammon, C., Vantelon, D., Chumakov A. I., et al. (2020). Determination of Fe3+/ΣFe of olivine-hosted melt inclusions using Mössbauer and XANES spectroscopy. *Chemical Geology.* doi: 10.1016/j.chemgeo.2020.119646

Galoisy, L. (2014). X-ray absorption spectroscopy in geosciences. In: *Spectroscopic methods in mineralogy* (pp. 553–587). EMU

notes in Mineralogy 6. https://doi.org/10.1180/EMU-notes.6.13

Galoisy, L., Calas, G., & Arrio, M. A. (2001). High-resolution XANES spectra of iron in minerals and glasses: structural information from the pre-edge region. *Chemical Geology*, *174*, 307–319. https://doi.org/10.1016/S0009-2541(00)00322-3

Geiger, C. A. (2004). An introduction to spectroscopic methods in the mineral sciences and geochemistry. In: *Spectroscopic Methods in Mineralogy*. Germany: Mineralogical Society of Great Britain and Ireland; 1–42. doi:10.1180/EMU-notes.6.1

Giuli, G., Paris, E., Hess, K.-U., Dingwell, D. B., Cicconi, M. R., Eeckhout, S. G., et al. (2011). XAS determination of the Fe local environment and oxidation state in phonolite glasses. *American Mineralogist*, *96*, 4. https://doi.org/10.2138/am.2011.3464

Giuli, G., Alonso-Mori, R., Cicconi, M. R., Paris, E., Glatzel, P., Eeckhout, S. G., & Scaillet, B. (2012a). Effect of alkalis on the Fe oxidation state and local environment in peralkaline rhyolitic glasses. *American Mineralogist*, *97*, 2–3. https://doi.org/10.2138/am.2012.3888

Giuli, G., Cicconi, M. R., & Paris, E. (2012b). The $^{[4]}Fe^{3+}$–O distance in synthetic kimzeyite garnet, $Ca_3Zr_2[Fe_2SiO_{12}]$. *European Journal of Mineralogy*, *24*, 5, 783–790. https://doi.org/10.1127/0935-1221/2012/0024-2206

Gonçalves Ferreira, P., de Ligny, D., Lazzari, O., Jean, A., Cintora Gonzalez, O., & Neuville, D. R. (2013). Photoreduction of iron by a synchrotron X-ray beam in low iron content soda-lime silicate glasses. *Chemical Geology*, *346*, 106–112. doi: 10.1016/j.chemgeo.2012.10.029

Harris, D. C., & Bertolucci, M. D. (1978). *Symmetry and Spectroscopy: An Introduction to Vibrational and Electronic Spectroscopy*. Oxford University Press, New York

Henderson, G. S., De Groot, F. M., & Moulton, B. J. (2014). X-ray absorption near-edge structure (XANES) spectroscopy. *Reviews in Mineralogy and Geochemistry*, *78*, 1, 75–138. doi: 10.2138/rmg.2014.78.3

Herzberg, G. (1945a). Molecular spectra and molecular structure. I. Spectra of diatomic molecule. Princeton Press.

Herzberg, G. (1945b). Molecular spectra and molecular structure. II. Infrared and Raman spectra of polyatomic molecules. Princeton Press.

Höche, T., Ikeno, H., Mäder, M., Blyth, R., Sales, B. C., & Tanaka, I. (2013). Vanadium L2,3 XANES experiments and first-principles multielectron calculations: Impact of second-nearest neighboring cations on vanadium-bearing fresnoites. *American Mineralogist*, *98*, 665–670. https://doi.org/10.2138/am.2013.4335

Höfer, H. E., Brey, G. P., Schulz-Dobrick, B., & Oberhänsly, R. (1994). The determination of the oxidation state of iron by the electron microprobe. *European Journal of Mineralogy*, *6*, 407–418. doi: 10.1127/ejm/6/3/0407

Hughes, E., Buse, B., Kearns, S., Blundy, J, Kilgour, G., Mader, H., et al. (2018). High spatial resolution analysis of the iron oxidation state in silicate glasses using the electron probe. *American Mineralogist*, *103*, 1473–1486. https://doi.org/10.2138/am-2018-6546CCBY

Hughes, E. C., Buse, B., Kearns, S. L., Brooker, R. A., Di Genova, D., Kilgour, G., et al. (2020). The microanalysis of iron and sulphur oxidation states in silicate glass - Understanding the effects of beam damage. IOP Conf. Series: Materials Science and Engineering 891, 012014 IOP Publishing - doi:10.1088/1757-899X/891/1/012014

Hunault, M. O. J. Y., Galoisy, L., Lelong, G., Newville, M., & Calas, G. (2016). Effect of cation field strength on Co2+ speciation in alkali-borate glasses. *Journal of Non-Crystalline Solids*, *451*, 101–110. https://doi.org/10.1016/j.jnoncrysol.2016.06.025

Jayasuriya, K. D., O'Neill, H.St.C., Berry, A. J., & Campbell, S. J. (2004). A Mössbauer study of the oxidation state of iron in silicate melts. *American Mineralogist*, *89*, 1597–1609. https://doi.org/10.2138/am-2004-11-1203

Kaindl, G., Wertheim, G. K., Schmiester, G., & Sampathkumaran, E. V. (1987). Mixed valency versus covalency in rare-earth core-electron spectroscopy. *Physical Review Letters*, *58*, 606–609. doi: 10.1103/PhysRevLett.58.606

Leister, M., Ehrt, D., Von der Goenna, G., Ruessel, C., & Breitbarth, F. (1999). Redox states and coordination of vanadium in sodium silicates melted at high temperatures. *Physics and Chemistry of Glasses*, *40*, 319–325.

Long, D. A. (1977). *Raman spectroscopy*. Great Britain, McGraw-Hill, Inc. 275 pp.

Le Losq, C., Neuville, D. R., Moretti, R., & Roux, J. (2012). Water quantification and speciation in silicate melt using Raman spectroscopy. *American Mineralogist*, *97*, 779–791.

Le Losq, C., Neuville, D. R., Moretti, R., Oppenheimer, C., & Kyle, P. (2015). Rheology of phonolitic magmas – the case of the Erebus lava lake. *Earth and Planetary Science Letters*, *411*, 53–61. https://doi.org/10.1016/j.epsl.2014.11.042

Le Losq, C., Berry, A. J., Kendrick, M. A., Neuville, D. R., & O'Neill, HSt. C. (2019). Determination of the oxidation state of iron in basaltic glasses by Raman spectroscopy. *American Mineralogist*, *104*, 1032–1042.

Le Losq, C., Moretti, R., Oppenheimer, C., Neuville, D. R. (2020). In situ XANES study of the influence of varying temperature and oxygen fugacity on iron oxidation state and coordination in a phonolitic melt. *Contributions to Mineralogy and Petrology*, *175*, 64–77. doi: 10.1007/s00410-020-01701-4

Lytle, F. W., van der Laan, G., Greegor, R. B., Larson, E. M., Violet, C. E., & Wong, J. (1990). Determination of the valence of Pr, Gd, and Ho in YBa2Cu3O7 by x- ray absorption spectroscopy. *Physical Review B*, *41*, 8955–8963. doi: 10.1103/physrevb.41.8955

Maeda, F., Kamada, S., Ohtani, E., Hirao, N., Mitsui, T., Masuda, R., et al. (2017). Spin state and electronic environment of iron in basaltic glass in the lower mantle. *American Mineralogist*, *102*, 2106–2112. https://doi.org/10.2138/am-2017-6035

Magnien, V. (2005). Etude cinétique des réactions d'oxydoréduction des silicates. PhD Institut de Physique du Globe de Paris. 284pp.

Magnien, V., Neuville, D. R., Cormier, L., Mysen, B. O., & Richet, P. (2004). Kinetics of iron oxidation in silicate melts: A preliminary XANES study. *Chemical Geology*, *213*, 253–263. https://doi.org/10.1016/j.chemgeo.2004.08.047

Magnien, V., Neuville, D. R., Cormier, L., Roux, J., Pinet, O., & Richet, P. (2006). Kinetics of iron redox reactions: A high-temperature XANES and Raman spectroscopy study. *Journal*

of Nuclear Materials, *352*, 190–195. doi: 10.1016/j.jnucmat.2006.02.053

Magnien, V., Neuville, D. R., Cormier, L., Roux, J., Hazemann, J.-L., de Ligny, D., et al. (2008). Kinetics and mechanisms of iron redox reactions in silicate melts: The effects of temperature and alkali cations. *Geochimica et Cosmochimica Acta*, *72*, 2157–2168. https://doi.org/10.1016/j.gca.2008.02.007

McMillan, P. F. (1984). A Raman spectroscopy study of glasses in the system CaO-MgO-SiO2. *American Mineralogist*, *69*, 645–659.

McMillan P. F. (1984). Structural studies of silicate glasses end melts – applications and limitations of Raman spectroscopy. *American Mineralogist*, *69*, 622–644.

McMillan, P. F., Piriou, B., & Navrotsky, A. (1982). A Raman spectroscopic study of glasses along the joins silica-calcium aluminate, silica-sodium aluminate and silica-potassium aluminate. *Geochimica et Cosmochimica Acta*, *46*, 2021–2037. https://doi.org/10.1016/0016-7037(82)90182-X

McMillan, P. F., Wolf, G. H., & Poe, B. T. (1992). Vibrational spectroscopy of silicate liquids and glasses. *Chemical Geology*, *96*, 351–366. https://doi.org/10.1016/0009-2541(92)90064-C

Metrich, N., Bonnin-Mosbah, M., Susini, J., Menez, B., & Galoisy, L. (2002). Presence of sulfite (S IV) in arc magmas: implications for volcanic sulfur emissions. *Geophysical Research Letters*, *129*, 11, 33-1–33-4. doi: 101029/2001GL014607

Metrich, N., Susini, J., Galoisy, L., Calas, G., Bonnin-Mosbah, M., & Menez, B. (2003). X-ray microspectroscopy of sulfur in basaltic glass inclusions. Influence on the volcanic sulfur emission. *Journal de Physique IV*, *104*, 393–397. doi: 10.1051/jp4:20030107

Möncke, D. (2018). Optical Spectroscopies. In: *The Encyclopedia of Archaeological Sciences* 1–7. John Wiley & Sons, Inc. https://doi.org/10.1002/9781119188230.saseas0423

Möncke, D., Papageorgiou, M., Winterstein-Beckmann, A., & Zacharias, N. (2014). Roman glasses coloured by dissolved transition metal ions: redox-reactions, optical spectroscopy and ligand field theory. *Journal of Archaeological Science*, *46*, 23–36. https://doi.org/10.1016/j.jas.2014.03.007

Mottana, A. (2014). X-ray absorption spectroscopy in mineralogy. In: Spectroscopic methods in mineralogy (pp. 465–552). EMU notes in Mineralogy 6. https://doi.org/10.1180/EMU-notes.6.12

Mysen, B. O. (1988). *Structure and properties of silicate melts*. Elsevier, Amsterdam. p. 354.

Mysen, B. O. (1990). Relationships between silicate melt structure and petrologic processes. *Earth-Science Reviews*, *27*, 281–365. https://doi.org/10.1016/0012-8252(90)90055-Z

Mysen, B. O. (1991). Relations between structure, redox equilibria of iron and properties of magmatic liquids. In: L. L. Perchuk and I. Kushiro (Eds.) *Physical chemistry of magmas, Advances in Physical Geochemistry, 9*, pp. 41–98. New York: Springer-Verlag.

Mysen, B. O., & Frantz, J. D. (1992). Raman spectroscopy of silicate melts at magmatic temperatures: Na2O-SiO2, K2O-SiO2 and Li2O-SiO2 binary compositions in the temperature range 25-1475°C. *Chemical Geology*, *96*, 321–332. https://doi.org/10.1016/0009-2541(92)90062-A

Mysen, B. O., & Frantz, J. D. (1994). Silicate melts at magmatic temperatures: in-situ determination to 1651°C and effect of temperature and bulk composition on the mixing behavior of structural units. *Contributions to Mineralogy and Petrology*, *117*, 1–14. https://doi.org/10.1007/BF00307725

Mysen, B. O., & Virgo, D. (1978). Influence of pressure, temperature and bulk composition on melt structures in the system NaAlSi2O6-NaFe3+Si2O6. *American Journal of Science*, *278*, 1307–1322.

Mysen, B. O., & Virgo, D. (1985). Iron-bearing silicate melts: relations between pressure and redox equilibria. *Physics and Chemistry of Minerals*, *12*, 191–200. https://doi.org/10.1007/BF00311288

Mysen, B. O., & Virgo, D. (1989). Redox equilibria, structure and properties of Fe-bearing alulminosilicate melts: relationships among temperature, composition and oxygen fugacity in system Na2O-Al2O3-SiO2-FeO. *American Mineralogist*, *74*, 58–76.

Mysen, B. O., Seifert, F. A., & Virgo, D. (1980). Structure and redox equilibria of iron-bearing silicate melts. *American Mineralogist*, *65*, 867–884.

Mysen, B. O., Virgo, D., & Kushiro, I. (1981). The structural role of aluminium in silicate melts – a Raman spectroscopy study at 1 atmosphere. *American Mineralogist*, *65*, 678–701.

Mysen, B. O., Virgo, D., & Seifert, F. A. (1982). Curve-fitting of Raman spectra of silicate glasses. *American Mineralogist*, *67*, 686–695.

Mysen, B. O., Virgo, D., & Seifert, F. A. (1982). The structure of silicate melts: implications for chemical and physical properties of natural magmas. *Reviews of Geophysics*, *20*, 353–383. https://doi.org/10.1029/RG020i003p00353

Mysen, B. O., Virgo, D., & Seifert, F. A. (1984). Redox equilibria of iron in alkaline earth silicate melts: relationships between melt structure, oxygen fugacity, temperature and properties of iron-bearing silicate liquids. *American Mineralogist*, *69*, 834–848.

Mysen, B. O., Virgo, D., & Seifert, F. A. (1985). Relationships between properties and structure of aluminosilicate melts. *American Mineralogist*, *70*, 88–105.

Mysen, B. O., Virgo, D., Neumann, E.-R., & Seifert, F. A. (1985). Redox equilibria and the structural states of ferric and ferrous iron in melts in the system CaO-MgO-SiO2-Fe-O: relationships between redox equilibria, melt structure and liquidus phase equilibria. *American Mineralogist*, *70*, 317–331.

Natoli, C. R. (1983). Near edge absorption structure in the framework of the multiple scattering model. Potential resonance or barrier effects? In: Bianconi, A., Incoccia, L., & Stilpich, S. (Eds.) *EXAFS and Near Edge Structure*, Springer Series in Chemistry and Physics, *27*, 43–56. Berlin: Springer.

Natoli, C. R., & Benfatto, M. (1986). A unifying scheme of interpretation of X-ray absorption spectra based on the multiple scattering theory. *Le Journal de Physique Colloques*, *47*, C8, C8-11-C8-23. https://doi.org/10.1051/jphyscol:1986802

Nesbitt, H. W., O'Shaughnessy, C., Bancroft, G. M., Henderson, G. S., & Neuville, D. R. (2018). Factors affecting line shapes and intensities of Q3 and Q4 Raman bands of Cs silicate glasses. *Chemical Geology*, *5*, 1–11. doi: 10.1016/j.chemgeo.2018.12.009

Neuville, D. R., & Mysen, B. O. (1996). Role of aluminium in the silicate network: in-situ, high temperature study of glasses and melts on the join SiO2-NaAlO2. *Geochimica et Cosmochimica Acta*, *60*, 1727–1737.

Neuville, D. R. (2006). Viscosity, structure and mixing in (Ca, Na) silicate melts. *Chemical Geology*, *229*, 28–42. https://doi.org/10.1016/j.chemgeo.2006.01.008

Neuville, D. R., Henderson, G. S., & de Ligny, D. (2014a). Advances in Raman spectroscopy applied to earth and material sciences. In: Henderson G. S., Neuville, D. R., Down, B. (Eds.) *Spectroscopic methods in Mineralogy and Material Sciences*, Review in Mineralogy and Geochemistry, Vol *78*, 509–541.

Neuville, D. R., Hennet, L., Florian, P., & de Ligny, D. (2014b). In situ high temperature experiment. In: Henderson, G. S., Neuville, D. R., & Down, B. (Eds.) *Spectroscopic methods in Mineralogy and Material Sciences*, Review in Mineralogy and Geochemistry, Vol *78*, 779–800.

Petit, P. E., Farges, F., Wilke, M., & Solé, V. A. (2001). Determination of the iron oxidation state in Earth materials using XANES pre-edge information. *Journal of Synchrotron Radiation*, *8*, 2, 952–954. doi: 10.1107/s0909049500021063

Pascal, P. (1958). *Nouveau traite de chimie minérale*. Masson edt.

Prieur, D., Epifano, E., Dardenne, K., Rothe, J., Hennig, C., Scheinost, A. C., et al. (2018). Negative thermal expansion of the UO2 fluorite local structure. *Inorganic Chemistry*. doi: 10.1021/acs.inorgchem.8b02657

Roskosz, M., Toplis, M. J., Neuville, D. R., & Mysen, B. O. (2008). Quantification of the kinetics of iron oxidation in silicate melts using Raman spectroscopy and assessment of the role of oxygen diffusion. *American Mineralogist*, *93*, 1749–1759. https://doi.org/10.2138/am.2008.2861

Rossman, G. R. (1988). Optical spectroscopy. *Reviews in Mineralogy*, *18*, 207–254.

Rossman, G. R. (2014). Optical spectroscopy. *Reviews in Mineralogy and Geochemistry*, *78*, 1, 371–398.

Soldatov, A. V., Ivanchenko, T. S., Della Longa, S., Kotani, A., Iwamoto, Y., & Bianconi, A. (1994). Crystal-structure effects in the Ce L3-edge x-ray-absorption spectrum of CeO2: Multiple-scattering resonances and many-body final states. *Physical Review B*, *50*, 8, 5074–5080. https://doi.org/10.1103/PhysRevB.50.5074

Seifert, F. A., Mysen, B. O., & Virgo, D. (1982). Three dimensional structure of quenched melts (glass) in the system SiO2-NaAlO2, SiO2-CaAl2O4 and SiO2-MgAl2O4. *American Mineralogist*, *67*, 696–717.

Takahashi, Y., Shimizu, H., Kagi, H., Yoshida, H., Usui, A., & Nomura, M. (2000a). A new method for the determination of CeIII/CeIV ratios in geological materials; application for weathering, sedimentary and diagenetic processes. *Earth and Planetary Science Letters*, *182*, 3–4, 201–207. https://doi.org/10.1016/S0012-821X(00)00250-8

Takahashi, Y., Shimizu, H., Usui, A., Kagi, H., & Nomura, M. (2000b). Direct observation of tetravalent cerium in ferromanganese nodules and crusts by X-ray-absorption near-edge structure (XANES). *Geochimica et Cosmochimica Acta*, *64*, 2929–2935.

Takahashi, Y. Kolonin, G. R., Shironosova, G. P., Kupriyanova, I. I., Uruga, T., & Shimizu, H. (2005). Determination of the Eu(II)/Eu(III) ratios in minerals by X-ray absorption near-edge structure (XANES) and its application to hydrothermal deposits. *Mineralogical Magazine 69*, 179–190. https://doi.org/10.1180/0026461056920245

Van Bokhoven, J. A., & Lamberti, C. (Eds.). (2016). *X-ray absorption and X-ray emission spectroscopy: theory and applications* (Vol. *1*). John Wiley & Sons.

Yaxley A., Berry, A. J., Rosenthal, A., Woodland, A. B., & Paterson, D. (2017). Redox preconditioning deep cratonic lithosphere for kimberlite genesis – evidence from the central Slave Craton. *Scientific Reports*, *7* 30. 10.1038/s41598-017-00049-3

Waychunas, G. A., Apted, M. J., & Brown, G. E. Jr. (1983). X-ray K-edge absorption spectra of Fe minerals and model compounds: near edge structure. *Physics and Chemistry of Minerals*, *10*, 1–9. https://doi.org/10.1007/BF01204319

Wang, Z., Cooney, T. F., & Sharma, S. K. (1995). In situ structural investigation of iron-containing silicate liquids and glasses. *Geochimica et Cosmochimica Acta*, *59*, 8, 1571–1577. https://doi.org/10.1016/0016-7037(95)00063-6

Wei, Q., McCammon, C., & Gilder, S.A. (2017). High-pressure phase transition of iron: A combined magnetic remanence and Mössbauer study. *Geochemistry, Geophysics, Geosystems*, *18*. doi: 10.1002/2017GC007143

Wildner, M., Andrut, M., & Rudowicz, C. Z. (2014). Optical absorption spectroscopy in geosciences. In: *Spectroscopic methods in mineralogy* (pp. 93–143). Germany: Mineralogical Society of Great Britain and Ireland. https://doi.org/10.1180/EMU-Notes.6.3

Wilke, M., Farges, F., Petit, P.-E., Brown, Jr G.E., & Martin, F. (2001). Oxidation state and coordination of Fe in minerals: An Fe K-XANES spectroscopic study. *American Mineralogist*, *86*, 714–730. https://doi.org/10.2138/am-2001-5-612

Wilke, M., Partzsch, G. M., Bernhardt, R., & Lattard, D. (2004). Determination of the iron oxidation state in basaltic glasses using XANES at the K-edge. *Chemical Geology*, *213*, 71–87. https://doi.org/10.1016/j.chemgeo.2005.03.004

Willmott, P. R. (2011). *An Introduction to Synchrotron Radiation: Techniques and Applications*. New York: John Wiley and Sons.

Wilson A. D. (1960). The micro-determination of ferrous iron in silicate minerals by a volumetric and colorimetric method. *Analyst*, *85*, 823–827. https://doi.org/10.1039/AN9608500823

Wilson, E. B., Decius, J. C., & Cross, P.C. (1955) *Molecular Vibrations: The Theory of infrared and Raman spectra*. New York: McGraw-Hill.

Wong, J., Lytle, F. W., Messmer, R. P., & Maylotte, D. H. (1984). K-edge absorption spectra of selected vanadium compounds. *Physical Review B*, *30*, 10, 5596–5610. https://doi.org/10.1103/PhysRevB.30.5596

Zhang, C., Almeev, R., Hughes, E. C., Borisov, A., Wolff, A., Höfer, H., et al. (2018). Electron microprobe technique for the determination of iron oxidation state in silicate glasses. *American Mineralogist*, *103*, 1445–1454. https://doi.org/10.2138/am-2018-6437

Zhang, H. L., Cottrell, E., Peat, S., Kelley, A. K., & Hirschmann, M. M. (2018). Determination of Fe3 +/ΣFe of XANES basaltic glass standards by Mössbauer spectroscopy and its application to the oxidation state of iron in MORB. *Chemical Geology*, *479*,166–175. https://doi.org/10.1016/j.chemgeo.2018.01.006